ELSEVIER

#### Contents lists available at ScienceDirect

# NeuroImage

journal homepage: www.elsevier.com/locate/ynimg





# Inter-regional correlation estimators for functional magnetic resonance imaging

Sophie Achard <sup>a,\*</sup>, Jean-François Coeurjolly <sup>a</sup>, Pierre Lafaye de Micheaux <sup>b,c,d</sup>, Hanâ Lbath <sup>a</sup>, Jonas Richiardi <sup>e</sup>

- <sup>a</sup> Univ. Grenoble Alpes, CNRS, Inria, Grenoble-INP, LJK, 38000 Grenoble, France
- <sup>b</sup> AMIS, Université Paul Valéry Montpellier 3, France
- <sup>c</sup> PreMeDICaL Precision Medicine by Data Integration and Causal Learning, Inria Sophia Antipolis, France
- <sup>d</sup> Desbrest Institute of Epidemiology and Public Health, Univ Montpellier, INSERM, Montpellier, France
- <sup>e</sup> Department of Radiology, Lausanne University Hospital and University of Lausanne, Switzerland

#### ARTICLE INFO

#### Keywords: Functional connectivity Correlation Aggregated data Familial correlations Serial correlations

#### ABSTRACT

Functional magnetic resonance imaging (fMRI) functional connectivity between brain regions is often computed using parcellations defined by functional or structural atlases. Typically, some kind of voxel averaging is performed to obtain a single temporal correlation estimate per region pair. However, several estimators can be defined for this task, with various assumptions and degrees of robustness to local noise, global noise, and region size.

In this paper, we systematically present and study the properties of 9 different functional connectivity estimators taking into account the spatial structure of fMRI data, based on a simple fMRI data spatial model. These include 3 existing estimators and 6 novel estimators. We demonstrate the empirical properties of the estimators using synthetic, animal, and human data, in terms of graph structure, repeatability and reproducibility, discriminability, dependence on region size, as well as local and global noise robustness.

We prove analytically the link between regional intra-correlation and inter-region correlation, and show that the choice of estimator has a strong influence on inter-correlation values. Some estimators, including the commonly used *correlation of averages* (cA), are positively biased, and have more dependence to region size and intra-correlation than robust alternatives, resulting in spatially-dependent bias. We define the new *local correlation of averages* estimator with better theoretical guarantees, lower bias, significantly lower dependence on region size (Spearman correlation 0.40 vs 0.55, paired t-test T=27.2,  $p=1.1e^{-47}$ ), at negligible cost to discriminative power, compared to the cA estimator.

The difference in connectivity pattern between the estimators is not distributed uniformly throughout the brain, but rather shows a clear ventral-dorsal gradient, suggesting that region size and intra-correlation plays an important role in shaping functional networks defined using the ca estimator, and leading to nontrivial differences in their connectivity structure. We provide an open source R package and equivalent Python implementation to facilitate the use of the new estimators, together with preprocessed rat time-series.

# 1. Introduction

Functional connectivity of the brain is estimated from observations using non invasive techniques such as electroencephalography (EEG), magnetoencephalography (MEG) or functional Magnetic Resonance Imaging (fMRI). Each recording provides time series associated to spatial locations within regions of the brain. Functional connectomes, that is, graphs representing the estimated connectivity, are then constructed by computing dependence measures between the time series. These connectomes are used in fundamental neuroscience, for example to study development (Fan et al., 2021; Tooley et al., 2021),

and in clinical neuroscience, to characterize psychiatric (Fornito et al., 2017) or neurological (Fornito et al., 2015) disorders. They form a compact yet expressive representation of brain activity that can be used for downstream analysis tasks such as diagnosis (Castellanos et al., 2013) or more generally machine learning approaches (Richiardi et al., 2013; Dadi et al., 2019).

For graph construction, typically, each region of the brain, defined by a structural or functional parcellation, is associated to a given set of voxels amongst the thousands for which a signal is recorded. The idea is then to extract a representative of the set of voxels to attach

E-mail address: sophie.achard@univ-grenoble-alpes.fr (S. Achard).

Corresponding author.

one time series to each region. When structural atlases are used, the most common approach is to take the average of the voxel time series at each time point. Indeed, almost 70% of papers on PubMed that used the Human Connectome Project dataset to conduct functional-connectivity-related studies in the last five years (e.g., Ogawa (2021), Figueroa-Jimenez et al. (2021), Bolt et al. (2017) and Zhang et al. (2016)) use this method (cf. Appendix A). While there are numerous other approaches to connectivity estimation (including the related techniques for estimating parcellation from connectivity, see, e.g., Eickhoff et al., 2015, or using regional medians Braun et al., 2012 or eigenvectors Büchel and Friston, 1997; Braun et al., 2012 instead of means), we focus on correlations between averaged regional time-courses, and argue that this technique introduces bias in the estimation of the functional connectomes.

The choice of acquisition sequence and hardware, physiological noise (Caballero-Gaudes and Reynolds, 2017), preprocessing (Braun et al., 2012), and subject motion all impact correlation estimators. Acquisition effects are site-dependent, causing heterogeneity problems in multi-site studies, although various harmonization techniques have been proposed as mitigation (Castrillon et al., 2014; Chen et al., 2022). In addition, it has been shown that computation of connectomes is affected by three main parameters: the length of the acquisition (Whitlow et al., 2011; Van Dijk et al., 2010), the number of regions (Stanley et al., 2013; Cao et al., 2019) and the chosen frequency band (Cordes et al., 2001; Salvador et al., 2005; Braun et al., 2012; Chen and Glover, 2015). Finally, sample size will also play a role in terms of group comparisons (Termenon et al., 2016).

Aggregation across voxels is often used because one wishes to increase the signal to noise ratio. This approach is also common in other areas of statistical analysis, for instance because the data are collected in different groups, organizations, or regions. However, difficult challenges arise due to the presence of correlations within the collected datasets.

Measurement errors can impact inter-region correlations. They have been well studied in fMRI, and are related to both the hardware and the subject (Greve et al., 2013). They are known to impart correlation structure to the data that is not linked to neural activity (Jo et al., 2010; Murphy et al., 2013), at various spatial scales. This problem is also common in other areas of statistical analysis. For example, Ostroff (1993) studied correlations between the score variables job satisfaction and technology (i.e., perception of the amount of standardization of tasks performed) both at the individual and organizational levels (individuals grouped into organizations such as companies). When organization-level estimates of correlation (i.e., correlations based on aggregated data) are obtained by averaging individual-level estimates of correlations, they showed that the ratio of individual to organizational correlations varied widely depending on measurement errors as well as other factors. This is an instance of the fallacy of the wrong level, when "correlations at a more macro level are used to make inference about individuals, or vice versa" (Ostroff, 1993).

Region size can also influence inter-region correlations. In fMRI, the dependence of inter-region correlations on brain region size has been noted (Achard et al., 2011), showing a positive relationship between region size and correlation values to the rest of the brain. This is particularly problematic because many atlases have some dependency between region size and spatial location (e.g. some deep gray matter structure may be parcellated into smaller regions or subregions than cortical structures). It has also been shown that temporal autocorrelation increases with region size, both for volume-based and surface-based parcellation (Afyouni et al., 2019), and that at a small scale regional homogeneity (Zang et al., 2004) – also called local connectivity and measured by the Kendall correlation coefficient of small neighborhood time series — is larger for 9-voxel than for 27-voxels neighborhoods (Jiang and Zuo, 2016).

In studies of familial data (Rosner et al., 1977), specific characteristics are obtained for different families with different sizes: *correlation* 

between the children and parents and the average of correlations between all children and parents are not equal in the majority of cases, due to differing number of children per family.

Finally, the spatial aspect of the data also complicates correlation estimation, in particular due to spatial autocorrelation between voxels (more simply named spatial correlation in the rest of the paper). Spatial correlation means that observations in neighboring voxels are not independent. However, independence is an assumption many statistical estimators rely on to simplify hypothesis testing by enabling the application of the central limit theorem, leading to false positives and artificially low p-values. Spatial correlation has been identified to be present in fMRI data previously, in particular in activation studies. Even if the methods to take into account the spatial correlation are different from the functional connectivity, it is worth detailing these specific approaches here. The common point between our problem in this paper and the activation studies is that spatial correlation has an impact on the design of the methodological approaches. Indeed, two classical approaches in fMRI activation studies are to either assume voxel independence, or conversely to smooth the data (Hartvig and Jensen, 2000). Smoothing itself can lead to location and amplitude mis-estimation (Descombes et al., 1998); alternatively, estimating smoothness from data allows adjusting effective number of degrees of freedom and reducing false positives, but can itself lead to variability in p-values from hypothesis tests (Poline et al., 1995). Spatial correlation has also been shown to deflate p-values in structural imaging (Burt et al., 2020), and has long been recognized as an issue in functional connectivity, for instance with early voxelwise (PET) connectivity approaches removing correlation "between neighboring voxels which can be attributed to spatial correlation" (Cao and Worsley, 1999). More recently, methods from spatial statistics have been applied for clustering fMRI data (Ye et al., 2009, 2011), and spatial correlation-preserving null models have been proposed to compare functional network maps (Alexander-Bloch et al., 2018; Markello and Misic, 2021) and thus avoid deflated p-values due to spatial correlation. Computing correlations is also common when geostatistics is applied to ecology, geography, climate studies, and more. The data collected in these fields are attached to a spatial position and usually with spatial correlation. The problem was first reported by Student (1914), and studied in Clifford et al. (1989) for two spatial processes. Applications of these methods can be found for example in the study of meteorological data (Gunst, 1995).

In all these fields of application, the main difficulty is to take into account spatial correlation when the goal is to construct estimators of correlation and to build testing procedures when the averaged variables are not independent.

In light of the above, preferable inter-correlation estimators should exhibit at least four properties (i) face validity, (ii) high repeatability, (iii) preservation of the differences between individuals (discriminative power), and (iv) independence from region size. In this paper, we question the default choice of using correlations of averages of voxel timecourses, and examine in details the assumptions of various methods and their robustness to various types of noise. We propose first a simple definition of a spatial model of fMRI with intra-correlations within brain regions. Then, computations of correlations are described and we show the potential bias in the estimators. Based on simulations, we illustrate the good behavior of the newly introduced estimators. Finally, we conclude with results on human data and rat data.

# 2. Proposed estimators of correlation

# 2.1. Definition of the proposed spatial model for fMRI data

Let  $\mathcal{C}\subset\mathbb{Z}^d$ ,  $d\in\mathbb{N}^*$ , be a finite compact set of multi-indices. In the context of our application, d=3 and  $\mathcal{C}$  contains all 3-tuples indexing the voxels of a three-dimensional image of a brain. Each brain is virtually partitioned into J regions of interest which are represented

through their subsets of voxels  $\mathcal{R}_j$  of cardinality  $\#\mathcal{R}_j=N_j,\,j=1,\ldots,J.$  We thus have

$$C = \bigcup_{j=1}^{J} \mathcal{R}_j$$
 and  $\#C = \sum_{i=1}^{J} N_j$ .

For any d-tuple  $i \in \mathcal{C}$ , a signal  $Y_i(\cdot)$  sampled at times  $t=1,\ldots,T$  is observed and we assume that it can be decomposed as follows

$$Y_i(t) = X_i(t) + \varepsilon_i(t) + e(t), \tag{1}$$

where  $X_i(\cdot)$  is an unobserved signal of interest,  $\varepsilon_i(\cdot)$  is a *local noise* contaminating locally the signal  $X_i(\cdot)$ , and  $e(\cdot)$  is a *global noise* corrupting in the same way the signal measured in each voxel indexed by an element of C. This can be, e.g., a consequence of thermal or background noise (Lazar, 2008; Greve et al., 2013), which at high field strength has been shown to explain a high proportion of noise variance (Greve et al., 2011).

We make a few assumptions on these different components. First, we assume that all random variables are centered. We also assume that the signals  $X_i(\cdot)$ ,  $\varepsilon_i(\cdot)$  and  $e(\cdot)$  are mutually independent and independent in time. This is not an overly restrictive assumption as for the applications presented in Section 3 we preprocess the data by applying a wavelet transform. And it is now well-known (Moulines et al., 2007), that if a random time series has short or long memory characteristics, after a wavelet decomposition, this signal can be approximated to be decorrelated in time for large wavelet scales. In addition, assuming that the  $X_i$ 's are centered is coherent as it is a well-known fact that a wavelet decomposition based on a wavelet mother with K vanishing moments cancels out every polynomial trend with degree K-1. Assuming that the local and global noises are homoskedastic with a variance denoted respectively by  $\sigma_{\epsilon}$  and  $\sigma_{e}$  is also not restrictive. Finally, we will be assuming (again following the literature Lazar, 2008; Greve et al., 2011, 2013) that the local noise  $\varepsilon$  is not too strongly spatially dependent and more precisely that two voxels far away have uncorrelated local noise. This is made more precise in Section 2.2.

#### 2.2. Spatial correlation structure induced by model (1)

Let  $i,i'\in C,\ j,j'=1,\ldots,J$   $(j\neq j')$  and for all  $t=1,\ldots,T$ , we assume that there exists  $\sigma_j>0,\ \sigma_\epsilon\geq 0,\ r_{jj'}\in [-1,1],\ \rho_{ii'}\in (0,1],\ \eta_{ii'}\in [-1,1]$  such that

$$\mathrm{E}[X_i(t)X_{i'}(t)] = \begin{cases} \sigma_j \sigma_{j'} r_{jj'} & \text{if } i \in \mathcal{R}_j, i' \in \mathcal{R}_{j'}, j \neq j', \\ \sigma_j^2 \rho_{ii'} & \text{if } i, i' \in \mathcal{R}_j \end{cases}$$

and

$$\mathrm{E}[\varepsilon_i(t)\varepsilon_{i'}(t)] = \sigma_\varepsilon^2 \eta_{ii'} \text{ if } i, i' \in \mathcal{R}_i.$$

The parameter  $r_{jj'}$  represents the correlation between two (unobserved) signals of two different regions  $\mathcal{R}_j$  and  $\mathcal{R}_{j'}$  and is called inter-correlation between regions  $\mathcal{R}_i$  and  $\mathcal{R}_{i'}$  in the following. This is the parameter of interest we focus on in the rest of the paper. The parameter  $\rho_{ii'}$  represents the intra-correlation between two (unobserved) signals inside a common region. Moreover, the parameter  $\eta_{ii'}$  represents the spatial correlation between two local noises inside a common region. We assume that inside each region, the signals of interest have positive intra-correlation. This is supported by literature (Uddin et al., 2008; Tomasi and Volkow, 2010; Jiang and Zuo, 2016). We also assume that for each time t and for j = 1, ..., J,  $\{X_i(t), i \in \mathcal{R}_i\}$  (resp.  $\{\varepsilon_i(t), i \in C\}$ ) is a second-order stationary and isotropic (with respect to the uniform norm) random field defined over  $R_i$  (resp. C). This means in particular that both the correlations  $\rho_{ii'}$  (for any  $i, i' \in \mathcal{R}_i$  for some j) and  $\eta_{ii'}$  (for  $i, i' \in \mathcal{C}$ ) depend only on the (uniform) distance (that is the usual distance on the lattice, e.g. Gaetan et al. (2010)) between the two voxels i and i'. For brevity, we still denote  $\rho_{|i'-i|}$  by  $\rho_{ii'}$  and  $\eta_{|i'-i|}$  by  $\eta_{ii'}$  where for  $x \in \mathbb{Z}^d$ , the notation |x| stands for the uniform norm. Our a priori hypothesis is that the intra-correlation  $\rho_{\delta}$  is close to 1 for moderate distances  $\delta$ , meaning that close neighbors are strongly (positively) correlated. Finally, we assume that the local noise is p-dependent, i.e.,  $\eta_{\delta}=0$  for any  $\delta>p$ . Without loss of generality, we also intrinsically assume that for all  $i\in\mathcal{R}_j$  and  $i'\in\mathcal{R}_{j'}$ ,  $\varepsilon_i(t)$  and  $\varepsilon_{i'}(t)$  are uncorrelated. This simplifies the presentation in the next sections. Furthermore, in the sequel, employing a slight abuse of language, we refer to the correlation between two voxels instead of the correlation between the signals originating from those voxels.

Hence, this results in the following (spatial) correlation structure for the signals  $Y_i$  and  $Y'_i$  at time t:

$$\mathrm{E}[Y_i(t)Y_{i'}(t)] = \begin{cases} \sigma_j \sigma_{j'} r_{jj'} + \sigma_e^2 & \text{if } i \in \mathcal{R}_j, i' \in \mathcal{R}_{j'}, j \neq j', \\ \sigma_j^2 \rho_{|i-i'|} + \sigma_\epsilon^2 \eta_{|i-i'|} + \sigma_e^2 & \text{if } i, i' \in \mathcal{R}_j \text{ and } |i-i'| \leq p \\ \sigma_j^2 \rho_{|i-i'|} + \sigma_e^2 & \text{if } i, i' \in \mathcal{R}_j \text{ and } |i-i'| > p. \end{cases}$$

Given a parcellation of the brain, the objective is to estimate intercorrelations  $r_{jj'}$  for each pair of regions of interest, independently of the parameters  $\sigma_j, \sigma'_j, \sigma_\varepsilon, \sigma_e, \rho_{ii'}, \eta_{ii'}$  which are viewed as nuisance parameters. We do not model the distribution of  $Y_i$  but only its second-order properties (through  $X_i, \varepsilon_i, e$ ). As said before, we consider the intra-correlations, the correlation of the local noise and the different variances as nuisance parameters that we do not want to estimate. In the next section, we present various estimators of  $r_{jj'}$  built in order to address one (or several) of the following cases: (1) the regions of interest  $\mathcal{R}_j$  and  $\mathcal{R}_{j'}$  may contain a different number of voxels; (2) the intra-correlation may deviate strongly from 1 (especially for large regions); (3) there may be a non negligible local noise  $\varepsilon_i$  affecting the signal in each region; (4) there may be a global noise affecting all regions.

## 2.3. Inter-correlation: notation and properties

Let  $\mathbf{Y}_1=(Y_1(1),\ldots,Y_1(T))$  and  $\mathbf{Y}_2=(Y_2(1),\ldots,Y_2(T))$  denote two voxel time-series of length T. The notation  $\widehat{\text{Cov}}(\mathbf{Y}_1,\mathbf{Y}_2)$ ,  $\widehat{\text{Cor}}(\mathbf{Y}_1,\mathbf{Y}_2)$  and  $\widehat{\sigma}^2(\mathbf{Y}_1)$  stand for the sample covariance between  $\mathbf{Y}_1$  and  $\mathbf{Y}_2$ , the sample correlation between  $\mathbf{Y}_1$  and  $\mathbf{Y}_2$  and the sample variance of  $\mathbf{Y}_1$ , respectively. For any  $j=1,\ldots,J$ , we define a  $\nu$ -neighborhood and denote it by  $\mathcal{V}$  as a subset of  $n_{\nu}:=(2\nu+1)^d$  indices, all of which are at a distance less than or equal to  $\nu$  from the center j of the neighborhood. For any set of indices E (which could be a  $\nu$ -neighborhood or a region of interest) and any spatio-temporal field  $Z_i(t)$  (which could be  $Y_i, X_i, \varepsilon_i, \ldots$ ) we denote by  $\tilde{Z}_E(t)$  for  $t=1,\ldots,T$  the time series spatially averaged over E, that is

$$\bar{Z}_E(t) = \frac{1}{\#E} \sum_{i \in E} Z_i(t).$$

To sum up, we reserve the bold notation to mainly denote a vector of length T, the notation  $\hat{\cdot}$  to denote an average over time while  $\bar{\cdot}$  will denote an average over space. Hence, for instance  $\hat{\sigma}^2(\bar{\mathbf{Y}}_E)$  denotes the sample variance of the vector with components  $(\#E)^{-1}\sum_{i\in E}Y_i(t)$  for  $t=1,\ldots,T$ . We also let

$$\bar{\rho}_E = \frac{1}{(\#E)^2} \sum_{i,i' \in E} \rho_{ii'}$$
 and  $\bar{\eta}_E = \frac{1}{(\#E)^2} \sum_{i,i' \in E} \eta_{ii'}$ . (2)

The quantity  $\bar{\rho}_E$  represents the (spatial) average intra-correlation inside the set E. If E corresponds to a v-neighborhood with moderate v, we may expect  $\bar{\rho}_{\mathcal{V}}$  to be close to 1. Such an observation is probably less realistic when  $E=\mathcal{R}_j$  especially for large regions. The quantity  $\bar{\eta}_E$  is related to the (spatial) correlation structure of the local noise. By assuming this noise to be p-dependent (that is  $\eta_{\delta}=0$  when  $\delta \geq p$ ), it is clear that the larger #E the smaller  $\bar{\eta}_E$ .

Using the assumption given in Section 2.1, for any  $E\subseteq \mathcal{R}_j$  and  $E'\subseteq \mathcal{R}_{j'}$ , we deduce

$$\operatorname{Cov}[\bar{Y}_E(t), \bar{Y}_{E'}(t)] = \begin{cases} \sigma_j \sigma_{j'} r_{jj'} + \sigma_e^2, & \text{if } j \neq j', \\ \sigma_i^2 \bar{\rho}_{E,E'} + \sigma_e^2, & \text{if } j = j', \end{cases}$$

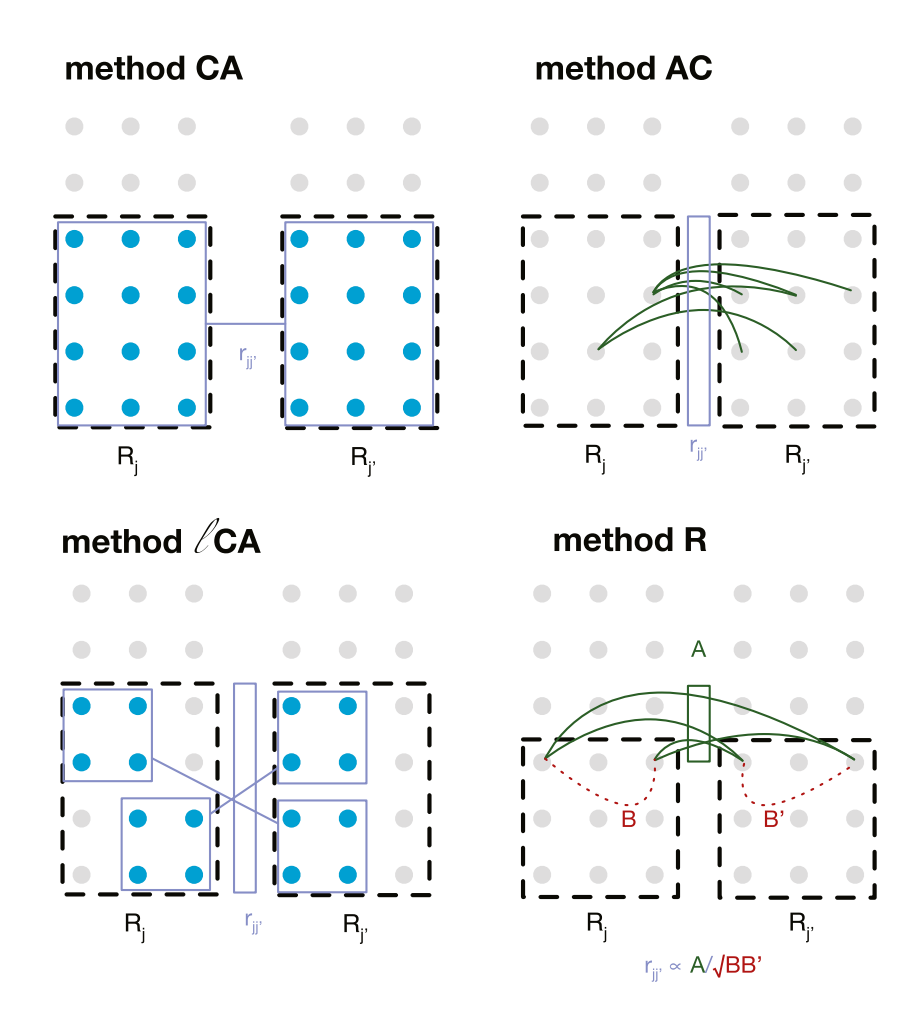


Fig. 1. Graphical overview of the inter-regional correlation estimators ca, ac,  $\ell$  ca, and R discussed in this paper. Gray dots represents voxels. Dashed black lines represent brain regions. Edges between voxels represent voxel-voxel temporal correlations. Blue rectangles show the region and level of aggregation (voxels or correlations).  $r_{ij'}$  shows quantities involved in the computation of the inter-regional correlations. Illustrations are approximate, please refer to the relevant equations for the exact definition. Neighborhood versions of the estimators (starting with  $\ell$ ) use the same principles but involve aggregating in small neighborhoods within regions.

where

$$\bar{\rho}_{E,E'} = \frac{1}{(\#E)(\#E')} \sum_{i \in E: i' \in E'} \rho_{|i-i'|}.$$

The variance can also be deduced as follows:

$$\operatorname{Var}[\bar{Y}_E(t)] = \sigma_i^2 \; \bar{\rho}_E + \sigma_\varepsilon^2 \; \bar{\eta}_E + \sigma_\varrho^2.$$

The detail of this result is given in Proposition C.1.

To lighten the expression of estimators proposed in the next sections, we define for  $j,j'\in\{1,\dots,J\}$ 

$$\sigma_{\varepsilon,j} = \frac{\sigma_{\varepsilon}}{\sigma_{j}}, \qquad \sigma_{e,j} = \frac{\sigma_{e}}{\sigma_{j}}, \qquad \text{and} \qquad \sigma_{e,jj'} = \frac{\sigma_{e}}{\sqrt{\sigma_{j}\sigma_{j'}}}.$$
 (3)

In the next sections, we set j,j' and thus aim to estimate  $r_{jj'}$  independently of the other parameters. The definition of standard estimators as well as novel estimators may look complicated due to the large amount of notation induced by the spatio-temporal correlation structure of Y and the methods themselves. However, we have postponed as much as possible theoretical contents to Appendix and present the estimation methods from an intuitive point of view in Figs. 1–2 in order to make next sections readable and reproducible.

# 2.4. Existing inter-correlation estimators

We first review existing inter-regional correlation estimators using a unified notation throughout.<sup>1</sup> Results on consistency of the estimators are provided in Appendices C–G.4.

# 2.4.1. Correlation of averages (method CA)

In order to increase the signal-to-noise ratio, the most standard method in fMRI is to average (or sometimes convolve with a Gaussian kernel) the signal in space (in each region of interest). The aggregated correlation estimator corresponds to the standard estimator (see Section 1) considered for example in Achard et al. (2006), Bolt et al. (2017) or Ogawa (2021):

$$\hat{r}_{jj'}^{cA} = \frac{\widehat{\text{Cov}}(\bar{\mathbf{Y}}_{R_j}, \bar{\mathbf{Y}}_{R_{j'}})}{\widehat{\sigma}(\bar{\mathbf{Y}}_{R_j})\widehat{\sigma}(\bar{\mathbf{Y}}_{R_{j'}})}.$$
(4)

 $<sup>^1</sup>$  In a previous study (Achard et al., 2011), we already described three of the estimators discussed here (ca, ac, &ca), but not with a unified notation, as well as a fourth estimator which is only discussed in the Appendix of the present paper.

This estimator, illustrated in Fig. 1 was designed to reduce the local noise. Indeed, in the absence of global noise  $(\sigma_e^2=0)$ , this estimator tends to  $r_{jj'}/\sqrt{(\bar{\rho}_{R_j}+\sigma_{\varepsilon,j}^2\bar{\eta}_{R_j})(\bar{\rho}_{R_j'}+\sigma_{\varepsilon,j'}^2\bar{\eta}_{R_j'})}$ . The interest of averaging before computing correlations is clear: the local noise is smoothed, thus  $\bar{\eta}_{R_j}=\mathcal{O}(1/N_j)$  is probably very small. However, even in absence of noise  $(\sigma_{\varepsilon}=\sigma_{e}=0)$ ,  $\hat{r}_{jj'}^{\text{CA}}$  has a serious drawback since it estimates  $r_{jj'}/\sqrt{\bar{\rho}_{R_j}\bar{\rho}_{R_{j'}}}$  which is highly dependent on intra-correlation. Just to give an example, assume  $r_{jj'}=1/2$ ,  $N_j=N_{j'}=2$ ,  $\rho_1=0$  then  $\bar{\rho}_{R_j}=\bar{\rho}_{R_{j'}}=1/2$  then  $\hat{r}_{jj'}^{\text{CA}}$  will converge towards 1 and not 1/2. This is a caricature but illustrates what may happen for large regions when some of the signals  $X_i$  are not enough positively intra-correlated. That fact was already pointed out by Achard et al. (2011).

#### 2.4.2. Average of correlations (method AC)

Instead of evaluating correlation of spatial averages, it is natural to perform the (spatial) average of correlations. This estimator, illustrated in Fig. 1, is given by:

$$\widehat{r}_{jj'}^{\text{AC}} = \frac{1}{N_j N_{j'}} \sum_{\substack{i \in R_j, \\ i' \in R_j,}} \widehat{\text{Cor}}(\mathbf{Y}_i, \mathbf{Y}_{i'}). \tag{5}$$

As seen from Table 1, in absence of global noise ( $\sigma_e^2=0$ ) and when the variances are equal to 1, this estimator estimates the quantity  $r_{jj'}/(1+\sigma_\epsilon^2)$  which makes this estimator robust to large regions (for which  $\bar{\rho}_{\mathcal{R}_j}$  may be far from 1) but more sensitive to local noise than the estimator  $\hat{r}_{ij'}^{\text{CA}}$ .

#### 2.4.3. Replicates for correlations (method R)

In order to cancel out the effect of local noise, we introduce to fMRI a slight adaptation of the estimator introduced by Bergholm et al. (2010), in the context of image analysis. This is based on the concept of replicates within the same region, and denoted by  $\hat{r}^R$  (R for replicates). The idea is to take two samples within each region, called replicates, to be able to compute correlation using these replicates to cancel out the local noise. These replicates can be chosen randomly a certain number of times denoted B. This estimator, illustrated in Fig. 1, is then obtained as a Monte-Carlo mean (or bootstrap) over different random replicates

$$\hat{r}_{jj'}^{R} = \frac{1}{B} \sum_{b=1}^{B} \frac{\frac{1}{4} \sum_{\alpha,\beta=1}^{2} \widehat{\text{Cor}}(\mathbf{Y}_{i_{\alpha}^{(b)}}, \mathbf{Y}_{i_{\beta}^{\prime(b)}})}{\sqrt{|\widehat{\text{Cor}}(\mathbf{Y}_{i_{1}^{(b)}}, \mathbf{Y}_{i_{2}^{\prime(b)}})|\widehat{\text{Cor}}(\mathbf{Y}_{i_{1}^{\prime(b)}}, \mathbf{Y}_{i_{2}^{\prime(b)}})|}}$$
(6)

where for  $b=1,\ldots,B$ ,  $i_1^{(b)},i_2^{(b)}\in\mathcal{R}_j$  are such that  $|i_2^{(b)}-i_1^{(b)}|=\delta\geq p$ . In the same way,  $i_1'^{(b)},i_2'^{(b)}\in\mathcal{R}_{j'}$  are such that  $|i_2'^{(b)}-i_1'^{(b)}|=\delta\geq p$ . Under equal variances and absence of global noise,  $\hat{r}_{jj}^R$  estimates  $1/|\rho_\delta|$  which is clearly independent of  $\sigma_\varepsilon^2$  and may be expected to be close to one if  $\delta$  is small.

#### 2.5. Novel estimators: discarding the effect of global and/or local noise

# 2.5.1. Use of a priori uncorrelated regions (method $\mbox{\tiny D}$ based on differences)

We now present an estimator which handles the problem of global noise. To achieve this task, we assume that among the regions where the signal is recorded there are at least two regions say  $\mathcal{R}_k$  and  $\mathcal{R}_{k'}$  which are uncorrelated between themselves and from all the other ones. With a slight abuse of notation, k,k' will be used for the indices of these two regions, while j,j' will be used when we are interested in the inter-correlation between regions  $\mathcal{R}_j$  and  $\mathcal{R}_{j'}$  (hence  $r_{jk}=r_{jk'}=r_{j'k}=r_{j'k}=r_{j'k'}=0$ ). This assumption is realistic in the context of fMRI data where we are interested in the correlations between cortical regions. Indeed, the field of view is typically larger than the brain itself, and the definition of extra regions is possible, for instance using air voxels or muscle voxels. The estimator is illustrated in Fig. 2.

We propose the following strategy: for b = 1, ..., B let  $i^{(b)}$ ,  $i'^{(b)}$ ,  $k^{(b)}$  and  $k'^{(b)}$  be voxels of  $\mathcal{R}_i$ ,  $\mathcal{R}_{i'}$ ,  $\mathcal{R}_k$  and  $\mathcal{R}_{k'}$ .

$$\hat{r}_{jj'}^{D} = \frac{1}{B} \sum_{b=1}^{B} \widetilde{\text{Cor}}(\mathbf{Y}_{i(b)}, \mathbf{Y}_{i'(b)}; \mathbf{Y}_{k(b)}, \mathbf{Y}_{k'(b)}),$$
(7)

where for four vectors  $\mathbf{Y}_1$ ,  $\mathbf{Y}_2$ ,  $\mathbf{Y}_3$  and  $\mathbf{Y}_4$  (with same length)

$$\widetilde{\text{Cor}}(\mathbf{Y}_{1}, \mathbf{Y}_{2}; \mathbf{Y}_{3}, \mathbf{Y}_{4}) = \frac{\widehat{\text{Cov}}(\mathbf{Y}_{1} - \mathbf{Y}_{3}, \mathbf{Y}_{2} - \mathbf{Y}_{4})}{\widehat{s}(\mathbf{Y}_{1}, \mathbf{Y}_{3}, \mathbf{Y}_{4}) \ \widehat{s}(\mathbf{Y}_{2}, \mathbf{Y}_{3}, \mathbf{Y}_{4})}$$
(8)

and where for three vectors U, V and W with same length

$$\widehat{s}^2(\mathbf{U},\mathbf{V},\mathbf{W}) = \left(\ \widehat{\sigma}^2(\mathbf{U}-\mathbf{V}) + \widehat{\sigma}^2(\mathbf{U}-\mathbf{W}) - \widehat{\sigma}^2(\mathbf{V}-\mathbf{W})\ \right)/2.$$

The intuition of this estimator is quite simple. Assume that the local noise has zero variance. Since the noise  $e(\cdot)$  is global, subtracting from  $Y_{i^{(b)}}(t)$  the value  $Y_{k^{(b)}}(t)$  and from  $Y_{j^{\prime}(b)}(t)$  the value  $Y_{k^{\prime}(b)}(t)$  discards the global noise. And since the regions  $\mathcal{R}_k$  and  $\mathcal{R}_{k^{\prime}}$  are not correlated and not correlated to the other ones, the numerator (for each b) is an estimate of  $\sigma_j\sigma_{j^{\prime}}r_{jj^{\prime}}$ . Then, we just have to divide by estimates of  $\sigma_j$  (and  $\sigma_{j^{\prime}}$ ). We observe that this cannot be done using simply  $\hat{\sigma}^2(\mathbf{Y}_{i^{(b)}}-\mathbf{Y}_{k^{(b)}})$  which estimates  $\sigma_j^2+\sigma_k^2+2\sigma_{\varepsilon}^2$ . This justifies the introduction of  $\hat{\tau}^2$ 

Note that  $\hat{r}_{jj'}^{D}$  is still biased with respect to local noise (see Table 1). An illustration of estimator D is provided in Fig. 2, and a more formal proposition and proof for this estimator are provided in Appendix E.

#### 2.5.2. Replicates and use of a priori disconnected regions: method RD

Combining replicates and the idea based on differences motivates us to propose the following estimator (see Sections 2.4.3 and 2.5.1 for notation)

$$\widehat{r}_{jj'}^{RD} = \frac{1}{B} \sum_{b=1}^{B} \frac{\frac{1}{4} \sum_{\alpha,\beta=1}^{2} \widetilde{\text{Cor}}(\mathbf{Y}_{i_{\alpha}^{(b)}}, \mathbf{Y}_{i_{j'}^{(b)}}; \mathbf{Y}_{k^{(b)}}, \mathbf{Y}_{k'^{(b)}})}{\sqrt{|\widetilde{\text{Cor}}(\mathbf{Y}_{i_{1}^{(b)}}, \mathbf{Y}_{i_{2}^{(b)}}; \mathbf{Y}_{k^{(b)}}, \mathbf{Y}_{k'^{(b)}}) \widetilde{\text{Cor}}(\mathbf{Y}_{i_{1}^{(b)}}, \mathbf{Y}_{i_{2}^{(b)}}; \mathbf{Y}_{k^{(b)}}, \mathbf{Y}_{k'^{(b)}})|}}$$
(9)

It is worth pointing out that  $r_{jj'}^{\rm RD}$  is independent of  $\sigma_{\varepsilon}$  and  $\sigma_{e}$  and equals the unknown  $r_{jj'}$  if  $\rho_{\delta}$  is close to 1. A more formal proposition and proof for this estimator are provided in Appendix F.

# 2.6. Localized versions of inter-correlation estimators

As mentioned previously, when noisy signals are averaged, the signal to noise ratio increases. A very popular method in neuroimaging analyses is to apply a Gaussian smoothing on the fMRI volumes (Worsley et al., 1992, 1996; Poline et al., 1997). However, applying a large kernel width may have dramatic effect on brain connectivity (Triana et al., 2020). Some earlier work on PET connectivity used a local neighborhood centered around voxels of interest to smooth the signal in each region prior to connectivity estimation (Köhler et al., 1998). We introduce in this section estimators using local neighborhoods to control the smoothing effect on correlation estimations.

# 2.6.1. Local correlation of averages (method $\ell$ CA)

Motivated by the first two estimators, we propose to estimate  $r_{jj'}$  using an empirical average of local spatial averages. For  $b=1,\ldots,B$ , let  $\mathcal{V}_i^{(b)}$  (resp.  $\mathcal{V}_{i'}^{(b)}$ ) be a v-neighborhood of  $\mathcal{R}_i$  (resp.  $\mathcal{R}_{i'}$ ). We define

$$\widehat{r}_{jj'}^{\text{CCA}} = \frac{1}{B} \sum_{b=1}^{B} \widehat{\text{Cor}}(\bar{\mathbf{Y}}_{\mathcal{V}_{j}^{(b)}}, \bar{\mathbf{Y}}_{\mathcal{V}_{j'}^{(b)}}). \tag{10}$$

#### method D

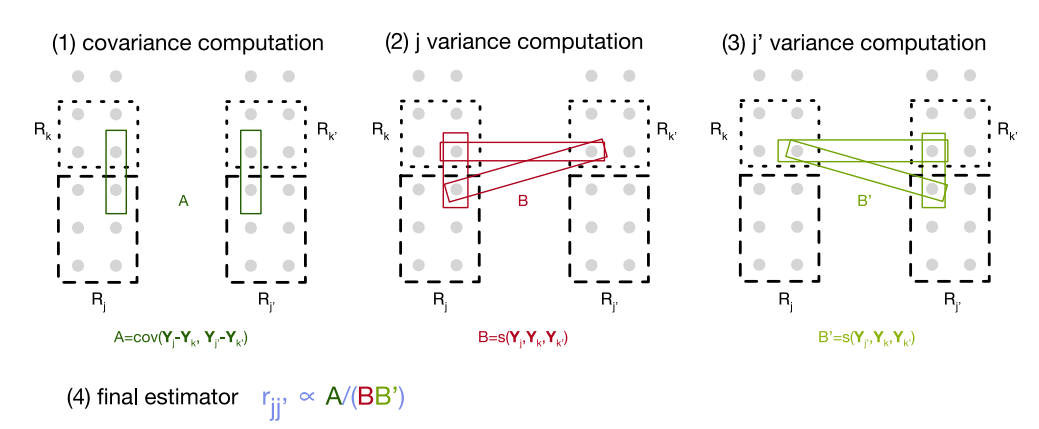


Fig. 2. Main steps involved in computing the inter-regional correlation estimator p. Dashed black lines represent brain regions of interest  $\mathcal{R}_j$  and  $\mathcal{R}_{j'}$ . Dotted black lines represent a priori uncorrelated region (e.g. air or muscle voxels)  $\mathcal{R}_k$  and  $\mathcal{R}_{k'}$ . Colored rectangles show the voxels involved in the computation. The final inter-regional correlation estimator  $r_{jj'}$  is defined in terms of the intermediate quantities computed in these three steps. See Fig. 1 for more details and other estimators.

#### 2.6.2. Local average of replicates (method $\ell$ R)

This estimator consists in replacing single indices by neighborhoods in (6). For  $b=1,\ldots,B$ , let  $\mathcal{V}_{j_1}^{(b)}$  and  $\mathcal{V}_{j_2}^{(b)}$  (resp.  $\mathcal{V}_{j_1'}^{(b)}$  and  $\mathcal{V}_{j_2'}^{(b)}$ ) be two vneighborhoods in  $\mathcal{R}_j$  (resp.  $\mathcal{R}_{j'}$ ) such that for any  $i_1^{(b)} \in \mathcal{V}_{j_1}^{(b)}$ ,  $i_2^{(b)} \in \mathcal{V}_{j_2}^{(b)}$ ,  $|i_1^{(b)}-i_2^{(b)}|=\delta \geq p$  for any  $i_1'^{(b)} \in \mathcal{V}_{j_1'}^{(b)}$ ,  $i_2'^{(b)} \in \mathcal{V}_{j_1'}^{(b)}$ ,  $i_2'^{(b)} \in \mathcal{V}_{j_1'}^{(b)}$ . The local average of replicates based estimator is defined by

$$\widehat{r}_{jj'}^{\ell R} = \frac{1}{B} \sum_{b=1}^{B} \frac{\frac{1}{4} \sum_{\alpha,\beta=1}^{2} \widehat{\text{Cor}}(\bar{\mathbf{Y}}_{\mathcal{V}_{j_{\alpha}}^{(b)}}, \bar{\mathbf{Y}}_{\mathcal{V}_{j_{\beta}}^{(b)}})}{\sqrt{|\widehat{\text{Cor}}(\bar{\mathbf{Y}}_{\mathcal{V}_{j_{1}}^{(b)}}, \bar{\mathbf{Y}}_{\mathcal{V}_{j_{2}}^{(b)}}) \widehat{\text{Cor}}(\bar{\mathbf{Y}}_{\mathcal{V}_{j_{1}'}^{(b)}}, \bar{\mathbf{Y}}_{\mathcal{V}_{j_{2}'}^{(b)}})|}}.$$
(11)

# 2.6.3. Local averages and use of disconnected regions (method $\ell_{\rm D}\!)$

We use in particular notation introduced in Sections 2.6.2 and 2.5.1 to propose the estimator  $\hat{r}_{ii'}^{\ell D}$  given by

$$\widehat{r}_{jj'}^{\ell D} = \frac{1}{B} \sum_{k=1}^{B} \widetilde{\text{Cor}}(\bar{\mathbf{Y}}_{\mathcal{V}_{j}^{(b)}}, \bar{\mathbf{Y}}_{\mathcal{V}_{j'}^{(b)}}; \bar{\mathbf{Y}}_{\mathcal{V}_{k}^{(b)}}, \bar{\mathbf{Y}}_{\mathcal{V}_{k'}^{(b)}}). \tag{12}$$

2.6.4. Replicates, local averages and use of a priori disconnected regions (method  $\ell_{RD}$ )

This estimator is a local version of  $\hat{r}_{ii'}^{RD}$  and is defined by

$$\hat{r}_{jj'}^{\ell RD} = \frac{1}{B} \sum_{b=1}^{B} \frac{\frac{1}{4} \sum_{\alpha,\beta=1}^{2} \widetilde{\text{Cor}}(\bar{\mathbf{Y}}_{\mathcal{V}_{j_{\alpha}}^{(b)}}, \bar{\mathbf{Y}}_{\mathcal{V}_{j_{\beta}}^{(b)}}; \bar{\mathbf{Y}}_{\mathcal{V}_{k'}^{(b)}}, \bar{\mathbf{Y}}_{\mathcal{V}_{k'}^{(b)}})}{\sqrt{\widetilde{\text{Cor}}(\bar{\mathbf{Y}}_{\mathcal{V}_{j_{1}}^{(b)}}, \bar{\mathbf{Y}}_{\mathcal{V}_{j_{2}}^{(b)}}; \bar{\mathbf{Y}}_{\mathcal{V}_{k'}^{(b)}}, \bar{\mathbf{Y}}_{\mathcal{V}_{k'}^{(b)}})} \cdot \widetilde{\text{Cor}}(\bar{\mathbf{Y}}_{\mathcal{V}_{j_{1}}^{(b)}}, \bar{\mathbf{Y}}_{\mathcal{V}_{j_{2}}^{(b)}}; \bar{\mathbf{Y}}_{\mathcal{V}_{k'}^{(b)}}, \bar{\mathbf{Y}}_{\mathcal{V}_{k'}^{(b)}})}.$$
(13)

#### 2.7. Summary of estimators

We have formalized 9 estimators for inter-region correlation in fMRI, 6 of which are novel to the best of our knowledge. They vary in terms of their theoretical sensitivity to three factors: differences in region sizes and region intra-correlations ( $\bar{\rho}_{R_j} \ll 1$ ), local noise ( $\sigma_{\varepsilon}$ ), and global noise ( $\sigma_{\varepsilon}$ ). Table 1 summarizes estimators properties qualitatively using — for estimators that are sensitive to these factors, + for estimators that are insensitive, and + for those that are inbetween. The CA,  $\ell$ CA, AC, and R estimators are sketched in Fig. 1 and the D estimator is illustrated in Fig. 2.

As an example, let us interpret the properties of CA shown in Table 1 in terms of these factors. First, we observe that the limit of  $\hat{r}^{\scriptscriptstyle{\text{CA}}}_{jj'}$  strongly

depends on the region size. Indeed, even in absence of noise this limit is  $r_{jj'}/\sqrt{\bar{\rho}_{R_j}\bar{\rho}_{R_{j'}}}$ , which can be quite far from  $r_{jj'}$  especially for very large regions (so the estimator is sensitive to local noise and denoted — in the corresponding column). Now imagine that  $\bar{\rho}_{R_j}\bar{\rho}_{R_{j'}}=1$  and that  $\sigma_e^2=0$  then the limit becomes  $r_{jj'}/\sqrt{(1+\sigma_{\epsilon_j}^2\bar{\eta}_{R_j})(1+\sigma_{\epsilon_{j'}}^2\bar{\eta}_{R_{j'}})}$ . Since it is expected that  $\bar{\eta}_E$  is small (see (C.3)), especially for large sets E, this limit should be quite close to  $r_{jj'}$  in this situation (+). Finally, if

this limit should be quite close to  $r_{jj'}$  in this situation (+). Finally, if  $\bar{\rho}_{R_j}\bar{\rho}_{R_{j'}}=1$  and  $\sigma_{\varepsilon}^2=0$ , and assume for simplicity that  $\sigma_j=\sigma_{j'}=1$ , then  $\hat{r}_{jj'}^{\text{CA}}$  would converge towards  $(r_{jj'}+\sigma_e^2)/(1+\sigma_e^2)$  which can significantly deviate from  $r_{jj'}$  when the global noise is strong (-). This does not describe at all finite sample properties of the different

This does not describe at all finite sample properties of the different estimators. Obviously, we could be tempted to always use the last two estimators (methods RD ad ℓRD) which seem to be the most robust to additional noises. However, these last estimators will be less robust to small sample size. We propose to investigate these finite sample properties in a simulation study (Section 3.1) and real datasets (Sections 3.2 and 3.3).

We note that evaluating asymptotic variances of the different estimators would add too much notation, assumptions and technicalities, and is left for future work.

#### 3. Description of simulated and real datasets

We employed three distinct datasets to assess the performance of our estimators. These datasets encompassed a simulated dataset, a dataset involving rats that comprised both deceased and living animals, and a dataset from a healthy human subject, which included test-retest data.

### 3.1. Simulated data

The paper being focused on pairwise spatial (auto)correlation estimation, it is sufficient to investigate the finite sample properties of our estimators for just two regions, say  $\mathcal{R}_j$  and  $\mathcal{R}_{j'}$  (whose sizes are set here to 20 and 40 voxels, respectively). Also, to save time and memory, we restrict ourselves, w.l.o.g., to one-dimensional regions (d=1, regions are simply intervals so they are simply made of 'voxels' along a line). For the estimators based on differences (methods  $\mathbf{D}, \ell \mathbf{D}, \ell \mathbf{R} \mathbf{D}$ ), we consider two extra regions, say  $\mathcal{R}_k$  and  $\mathcal{R}_{k'}$ , that are disconnected (i.e.,  $r_{jk} = r_{jk'} = r_{jk'} = r_{j'k} = r_{j'k'} = 0$ ). We consider two scenarios: the "relatively strong inter-correlation case"  $(r_{jj'} = 0.6)$  and the "no inter-correlation case"  $(r_{jj'} = 0)$ . The intra-correlation for any given

Table 1

Expected limits and properties for existing and novel estimators of inter-correlation  $r_{JJ'}$ , under the model (1). We refer the reader to Section 2.3 for details on notation. In particular  $\sigma_{e,J}^2$ ,  $\sigma_{e,J}^2$  and  $\sigma_{e,JJ'}^2$  are given by (3) while  $\bar{\rho}_E, \bar{\eta}_E$  and  $\bar{\rho}_{E,E'}$  for two sets of indices E, E' are given by (2) and (C.7). Sensitivity of estimators to three factors are reported: differences in region sizes and region intra-correlations ( $\bar{\rho}_{R_J} \ll 1$ ), local noise ( $\sigma_{e}$ ), and global noise ( $\sigma_{e}$ ). Estimators that are sensitive to these factors are denoted — those that are insensitive are denoted + and those in-between are denoted insensitive +

Estimator	Limit $r_{jj'}^{\bullet}$	Sensitivity to		
		$\bar{\rho}_{R_j} \ll 1$	$\sigma_{\varepsilon}$	$\sigma_e$
$\hat{r}^{\text{CA}}$ (see (4))	$\frac{r_{j,l'} + \sigma_{c,j,l'}^2}{\sqrt{(\bar{\rho}_{R_j} + \sigma_{c,j}^2 \bar{\eta}_{R_j} + \sigma_{c,j}^2)(\bar{\rho}_{R_{j'}} + \sigma_{c,j'}^2 \bar{\eta}_{R_{j'}} + \sigma_{c,j'}^2)}}$	_	+	_
$\hat{r}^{AC}$ (see (5))	$\frac{r_{jj'} + \sigma_{e,jj'}^2}{\sqrt{(1 + \sigma_{e,j}^2 + \sigma_{e,j}^2)(1 + \sigma_{e,j'}^2 + \sigma_{e,j'}^2)}}$	+	_	_
$\hat{r}^{\ell CA}$ (see (10))	$\frac{r_{jj'} + \sigma_{e,jj'}^2}{\sqrt{(\bar{\rho}_{V} + \sigma_{e,j}^2 \bar{\eta}_{V} + \sigma_{e,j}^2)(\bar{\rho}_{V} + \sigma_{e,j'}^2 \bar{\eta}_{V} + \sigma_{e,j'}^2)}}$	+	±	_
$\hat{r}^{R}$ (see (6))	$\frac{r_{jj'} + \sigma_{c,jj'}^2}{\sqrt{ (\rho_{\delta} + \sigma_{c,j}^2)(\rho_{\delta} + \sigma_{c,j'}^2) }}$	+	+	_
$\hat{r}^{\ell R}$ (see (11))	$\frac{r_{jj'} + \sigma_{e,jj'}^2}{\sqrt{ (\bar{\rho}_{\mathcal{V},\mathcal{V}^j,\delta} + \sigma_{e,j}^2)(\bar{\rho}_{\mathcal{V},\mathcal{V}^j,\delta} + \sigma_{e,j'}^2) }}$	+	+	_
$\hat{r}^{\mathrm{D}}$ (see (7))	$\frac{r_{jj'}}{\sqrt{\left(1+\sigma_{\varepsilon,j}^2\right)\left(1+\sigma_{\varepsilon,j'}^2\right)}}$	+	_	+
$\hat{r}^{\ell D}$ (see (12))	$\frac{r_{jj'}}{\sqrt{(\bar{\rho}_{V}+\sigma_{e,j}^{2}\bar{\eta}_{V})(\bar{\rho}_{V}+\sigma_{e,j'}^{2}\bar{\eta}_{V})}}$	+	±	+
$\hat{r}^{\mathrm{RD}}$ (see (9))	$\frac{1}{ \rho_{\delta} }$	+	+	+
$\hat{r}^{\ell \text{RD}}$ (see (13))	$\frac{1}{ \bar{\rho}_{\mathcal{V},\mathcal{V}',\delta} }$	+	+	+

region is modeled (alike within any region  $\mathcal{R}_j, \mathcal{R}_{j'}, \mathcal{R}_k, \mathcal{R}_{k'}$ ) using the following spatial model

$$\rho_{ii'} = 1 - (1 - \nu) \left( 1 - \frac{|i - i'|}{40} \right) \tag{14}$$

which only depends on the distance |i-i'| between two voxels, say i and i', belonging to the same region. We selected either the value v=0.8 or v=0, and designated accordingly the region as strongly or weakly intra-correlated. Hence, when v=0, the two voxels furthest apart in the region of size 40 are uncorrelated, i.e.,  $\rho_{ii'}=0$  when |i-i'|=40. When v=0.8, they are highly correlated with  $\rho_{ii'}=0.8$ . Fig. 3 represents the correlation structure of (14), as well as the quantity  $\bar{\rho}_E$  for sets of indices  $E\subseteq\{1,\dots,40\}$  with increasing size #E, for both intra-correlation models. We generated independently 500 series of length T=1000 according to model (1), and used 500 replicates for the method R and also 500 (Monte-Carlo or bootstrap) replications of choices of neighborhoods for methods  $\ell_{CA}$ ,  $\ell_{R}$ ,  $\ell_{D}$ ,  $\ell_{RD}$  (where we set the length of the neighborhood to 3). The local noises  $\varepsilon_i(t)$  and  $\varepsilon_{i'}(t)$  are assumed to be uncorrelated, so for some set of indices E,  $\bar{\eta}_E=\sigma_e/\#E$ . This is also represented in Fig. 3.

Finally, we chose two values for the variance of the global noise,  $\sigma_e^2=0$  and  $\sigma_e^2=0.1$ , and two values for the variance of the local noise,  $\sigma_e^2=0$  and  $\sigma_e^2=0.1$ . Results consist of 500 estimates for 9 methods, 2 intra-correlation models, 2 values for  $\sigma_e^2$  and 2 values for  $\sigma_e^2$ , that is 16 different scenarii (involving each time the 9 methods). They are presented and discussed in Section 6.1.

# 3.2. Rats data

Using a 9.4T machine (Paravision 6.0.1, Bruker, Ettlingen, Germany), fMRI data were acquired for both dead and alive rats in Pawela et al. (2008). Twenty-five rats were scanned and identified in 4 different groups: DEAD, ETO-L (Etomidate), ISO-W (Isoflurane) and MED-L(Medetomidine). The first group contains dead rats and the three last groups correspond to different anesthetics. In this paper, we show results with data from three rats, one dead and two alive with different anesthetics (ETO-L, ISO-W).

The duration of the scanning was 30 min, using single-shot echoplanar imaging with TR/TE = 500/20 ms, so that 3600 time points were available at the end of experiment. The resolution was  $0.47 \times 0.47 \times 1.00$  mm, slice gap 0.1 mm, 9 slices. After preprocessing as explained in Becq et al. (2020b), 51 brain regions for each rat were extracted using an in-house atlas. Sufficiently large regions are needed to be able to use the R estimator. We hence discarded regions that contained fewer than 40 voxels, and were left with 18 brain regions: The anterior cingulate cortex (ACC), bilateral Insular cortex (Ins\_r and Ins\_l), bilateral primary motor cortex (M1\_r and M1\_l), bilateral somatosensory 1 (S1\_r and S1\_l), bilateral somatosensory 1 barrel field (S1BF\_r and S1BF\_l), bilateral auditory cortex (AU\_r and AU\_l), bilateral caudate-putamen (striatum) (CPu\_r and CPu\_l), bilateral thalamus (Th\_r and Th\_l), bilateral basal forebrain region (BF\_r and BF\_l), bilateral hippocampus (HIP\_r and HIP\_l).

Voxel time series were wavelet-filtered using Daubechies orthonormal compactly supported wavelet of length 8.

#### 3.3. Human connectome project data

We also evaluated our estimators on a subset of the Human Connectome Project (HCP) Young Adult 1200 Subjects release, WU-Minn Consortium pre-processed (Glasser et al., 2013) (connectome db data package *Resting State fMRI 1/2 Preprocessed*). We selected 100 subjects with two rs-fMRI acquisitions on different days. The TR was 720 ms and the duration of acquisition was 14 min and 24 s.

The preprocessed fMRI data was segmented into 89 regions with SPM *New Segment* using a modified AAL template: merging some of the regions, reducing the parcellation to 89 regions. Merged regions are: frontal medial orbital and rectus (one region for left and one for right hemisphere); occipital superior, middle and inferior (one region for left and one for right hemisphere); temporal pole superior and medial (one region for left and one for right hemisphere); the cerebral crus (one region for left and one for right hemisphere); areas III, IV, V and VI of cerebellum (one region for left and one for right hemisphere); areas VII, VIII, IX, X of cerebellum (one region for left and one for right hemisphere) and finally, the vermis (one single region for both hemispheres). Other details are available in Termenon et al. (2016).

Voxel time series were wavelet filtered using Daubechies orthonormal compactly supported wavelet of length 8.

# 4. Evaluation and metrics

First, on *simulated data*, we qualitatively inspected the bias and variance of the distribution of correlation values with respect to known ground truth for various levels of global and local noise.

Then, using *rat data*, we performed a face validity analysis of the estimators, with the premise that dead rats should show no functional connectivity (the correlation distribution should be centered at zero). In order to quantify the differences between correlation values obtained for dead and live rats, we computed the Wasserstein distance between the correlation distributions of each anesthetized rat in comparison to that of a dead rat. A low value of the Wasserstein distance indicates that correlations values of live and dead rats are comparable and counts negatively in the evaluation of an estimator.

To evaluate the repeatability of the proposed estimators on the rat dataset, we split the time series in two equal parts. We computed the correlations on each part using the whole range of proposed estimators, and computed the Concordance Correlation Coefficient (CCC) (Lin, 1989) between splits to provide a scaled measure of agreement, where 1 is perfect agreement and 0 is no agreement. A preferable estimator should be more repeatable and have higher CCC.

To quantify the similarity of connectivity graphs between estimators, we computed the number of common edges between graphs obtained from each estimator. To this end we used a sparsity threshold

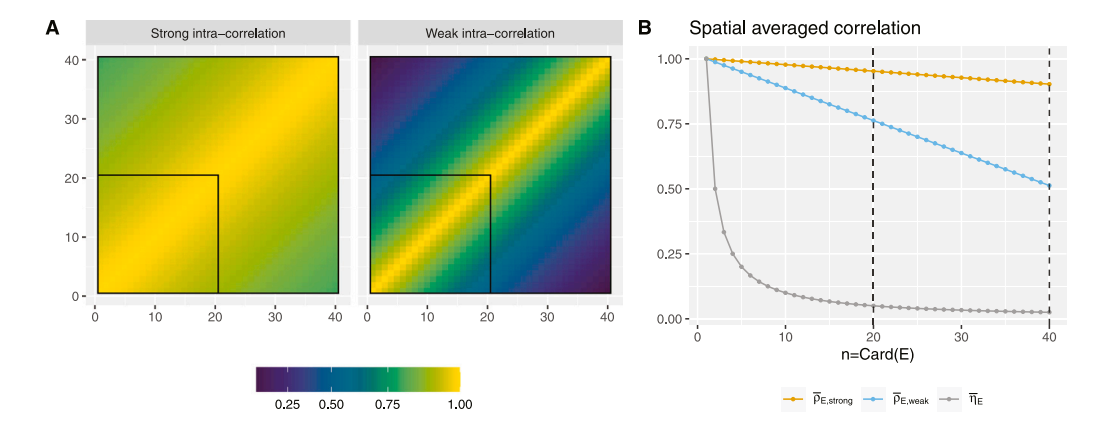


Fig. 3. Simulation setup and results. (A) The two simulated one-dimensional regions (one with 40 "voxels", the other with 20 "voxels", shown as an inset) and their intra-correlation structure. Intra-correlation  $\rho_{ii'}$  is given by (14) (with  $\nu=0.8$  for the strong intra-correlation and  $\nu=0$  for the weak intra-correlation) and decays with distance. (B) Intra-correlation (vertical axis) as a function of the size of region E (horizontal axis). From top to bottom:  $\bar{\rho}_E$  (orange): average intra-correlation of signal in the strong case;  $\bar{\rho}_E$  (blue): average intra-correlation of signal in the weak case;  $\bar{\eta}_E$  (black): average intra-correlation of noise. Average noise intra-correlation decays sharply with region size.

equal to 20% of the total number of edges (i.e., 27 edges in our case with 18 regions).

For human data, we used rs-fMRI sessions from different days, in order to evaluate reproducibility of correlation coefficients. This was analyzed using CCC, again with a preferable estimator being more reproducible and having higher CCC.

We also evaluated the reproducibility of graph metrics between sessions. To this end we used a sparsity threshold equal to 20% of the total number of edges, keeping only edges with the highest correlation (i.e., 783 edges in our case with 89 regions), and binarized the edges. In order to compute graph metrics, we forced the graph to be connected by applying a minimum spanning tree (Alexander-Bloch et al., 2010). Then we computed classical graph metrics: betweenness centrality, transitivity, global and local efficiencies using package iGraph. Reproducibility was evaluated using the CCC.

We also summarized the differences of connectivity graphs between estimators, by computing the number of common edges between graphs obtained from CA and &CA using thresholding at the 20th percentile (i.e., 783 edges with 89 regions), and visualized the difference qualitatively by taking absolute values of correlation values for each estimator, rank-transforming, and computing median difference in ranks across all subjects,

Additionally, we also evaluated discriminative power of the various estimators via three metrics: inter vs. intra-subject graph distance, a non-parametric test of the same, and identification rate using functional connectome fingerprinting (Finn et al., 2015). A desirable estimator should provide estimates that preserve inter-individual differences.

We defined the intra-subject distance as the distance between the graph representing the first rs-fMRI session and the graph representing the second rs-fMRI session. The inter-subject distance was computed between each subject's first session and all other subject's first sessions. Separation between the intra-subject distances and the inter-subject distances was quantified by mean and standard deviation of the distributions, and by a Wilcoxon rank-sum test on multiple random splits of subject data, to avoid having multiple measurements of the same subjects. Here, we repeated 10 times the following procedure for each estimator of interest: first, split the subjects into two disjoint sets one used to compute intra-distances (50 subjects), and one to compute inter-distances (50 subjects). Within the inter-distances set, 25 subject pairs were formed randomly. We tested the null hypothesis of no difference between inter- and intra-distances, against the alternative hypothesis that intra-subject distance < inter-subject distance, based on the assumption that subjects are more similar to themselves than to other subjects. Given the relatively narrow age range of our sample of HCP subjects (all 22-35 except one 36+), and given that our goal

was to compare estimators using fixed splits, we did not adjust for covariates or match samples across splits We used a one-sided Wilcoxon rank-sum test, yielding a W statistic and a p-value for each of the 10 runs. We then computed the average W value across runs, as well as the harmonic mean p-value (Wilson, 2019) across runs, a procedure with strong family-wise error rate (FWER) control even for positively dependent tests.

To compute identification rate, functional connectome fingerprinting represent each subject's graph g as a vectorized version  $\mathbf{a}$  of the upper-triangular (or lower-triangular) part of the full inter-region correlation matrix (whose entries are  $r_{ii'}$ ), and computes the fingerprinting distance between graphs as  $d(g_1,g_2)=1-\widehat{\text{Cor}}(\mathbf{a}_1,\mathbf{a}_2)$ , where Cor denotes Pearson correlation. From the (intra, inter) fingerprinting distance distributions, the identification counts as correct if the intra-subject distance is lower than all inter-subject distances. This is equivalent to a top-1 recognition rate. We note there are many other possibilities to compute distances between such brain graphs (Richiardi et al., 2013; Ng et al., 2016; Dadi et al., 2019), including computing distances between graph embeddings, which could substantially alter results.

Finally, we evaluated the dependence on region size by computing Spearman correlations between atlas region size and the average of correlations in which the region is involved (itself averaged across subjects). A preferable estimator should minimize dependence to region size, and show lower Spearman correlation. We tested differences between estimators using a paired t-test between these Spearman correlations.

#### 5. Data and code availability

R and Python code implementing all estimators, to generate simulated data, and to extract the time-series from the preprocessed HCP data is available at https://gitlab.inria.fr/q-func/ireco4fmri.

The pre-extracted, wavelet-filtered time series for the rat data are available at https://dx.doi.org/10.5281/zenodo.7254133. Human Connectome Project data is available at https://www.humanconnectome.org/.

#### 6. Results

# 6.1. Evaluation on simulated data

Simulation setup is described in Section 3.1. Fig. 4 shows boxplots of estimates of  $r_{jj'}=0.6$  for all methods and different intra-correlation models, and different levels of local and global noise. In terms of bias, overall, the method  $\ell$ RD is the best, but it is also the one with

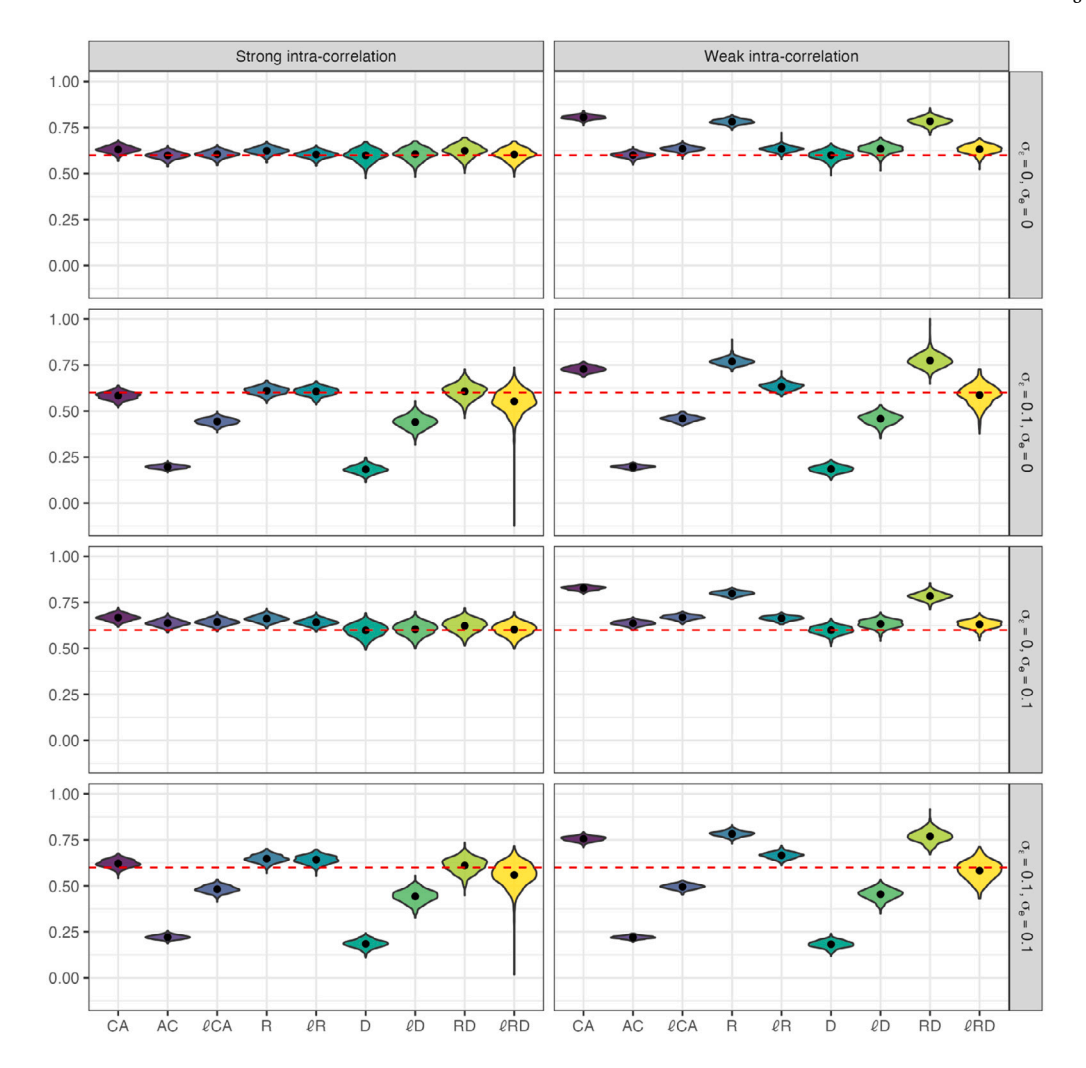


Fig. 4. Estimates of the inter-correlation parameter  $r_{jj'} = 0.6$  between two regions, based on 500 simulation runs of the general model (1). Situations for two intra-correlation models and situations with no noise, local noise and/or global noise are considered. The true inter-correlation is depicted by a red dashed line.

the highest variance. In the strong intra-correlation case, and when  $\sigma_{\varepsilon}=0$ , all methods are almost unbiased. When  $\sigma_{\varepsilon}$  is increased to 0.1, the estimators  $_{\text{AC}}$ ,  $_{\text{CA}}$ , D, and  $_{\text{CD}}$  clearly lose this property. In the weak intra-correlation case, only the estimators  $_{\text{AC}}$ ,  $_{\text{CR}}$  and  $_{\text{CR}}$  are unbiased, or close to, with  $_{\text{CRD}}$  being the best overall for this criterion, while still being the more variable. Fig. 5 shows boxplots of estimates of  $r_{jj'}=0$  for all methods and different intra-correlation models, and different levels of local and global noise. When  $\sigma_{e}=0$  all estimators are unbiased, both in the strong and weak intra-correlation case. This property remains true when  $\sigma_{e}$  is increased to 0.1 only for the estimators D,  $_{\text{CD}}$  and RD. Here again, the estimator  $_{\text{CRD}}$  is the more variable. We can also notice that when  $\sigma_{\varepsilon}=0.1$ , the estimator  $_{\text{CRD}}$  exhibits very good properties, while  $_{\text{CRD}}$  is the worst.

#### 6.2. Evaluation on rat data

Fig. 6(A) shows the correlation values obtained on rats for all pairs of brain regions, 153 in our case. For this data set, we know that for the dead rat we are under the full null hypothesis as no legitimate functional activity should be detected. Thus the estimated correlations should be close to zero. This is the case for estimators AC, R,  $\ell CA$ , D and  $\ell D$ . However, the other estimators showcase a clear bias towards positive values. The method CA namely yields unexpectedly high values of correlations. These correlations correspond to regions

that are close together (Becq et al., 2020a). In order to validate these methods, we also apply our estimators to live rats. The results of two live rats is shown in Fig. 6(A, right). As expected, due to the local noise, the methods  $_{AC}$  and  $_{D}$  do not provide satisfactory results as the correlation values are very close to zero. One of the best method in this case is  $_{CA}$ , where sufficient non-zero correlations are obtained. Wasserstein distance computations (Fig. 6(C)) show that  $_{AC}$ ,  $_{D}$ , and  $_{RD}$  have the lowest Wasserstein distance values, indicating that the correlation distribution of the live rats resemble that of a dead rat.

Fig. 6(B) shows Concordance Correlation Coefficient results. Consistent with the all-noise nature of the data, the dead rat exhibited very low repeatability, with  $\ell_{CA}$  providing the highest at 0.22. On the live Eto-L rat, estimators had approximately the same repeatability, with RD showing the lowest CCC at 0.62 and AC tied with  $\ell_{CA}$  for highest at 0.87. For the Iso-W rat,  $\ell_{R}$  had the lowest CCC at 0.46, CA the second lowest at 0.54, and  $\ell_{D}$  the highest at 0.73.

Combining all of these results,  $\ell_{CA}$ , R and  $\ell_D$  hence seem to be the most adequate correlation estimators. However, as shown in formula (G.4), the estimator  $\ell_D$  is difficult to implement. Indeed, it requires the definition of two other regions uncorrelated with the main brain regions of the parcellation and uncorrelated with themselves. Moreover, R cannot be estimated when regions are too small, which is often the case in rat data. From now on, we will hence focus on estimator  $\ell_{CA}$ .

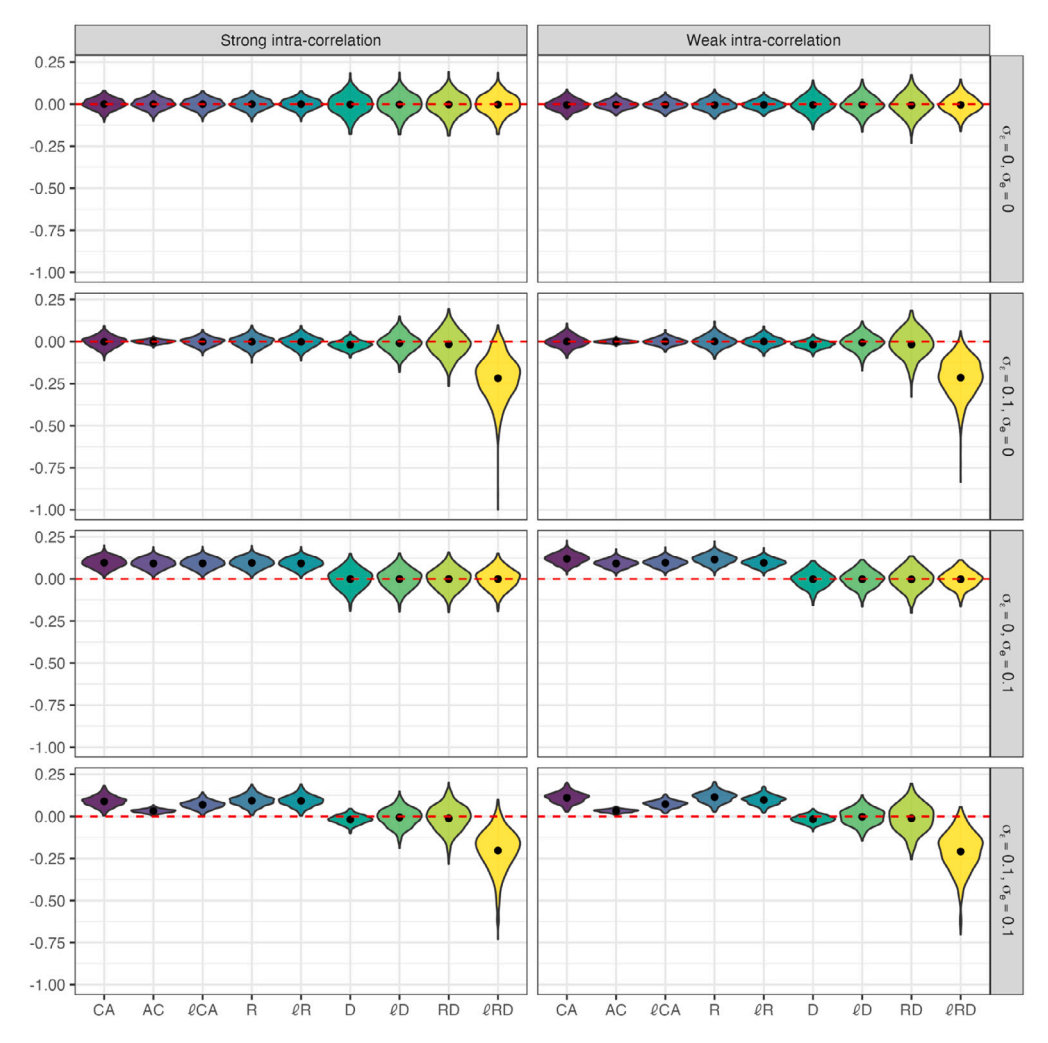


Fig. 5. Estimates of the inter-correlation parameter  $r_{jj'} = 0$  between two regions, based on 500 simulation runs of the general model (1). Situations for two intra-correlation models and situations with no noise, local noise and/or global noise are considered. The true inter-correlation is depicted by a red dashed line.

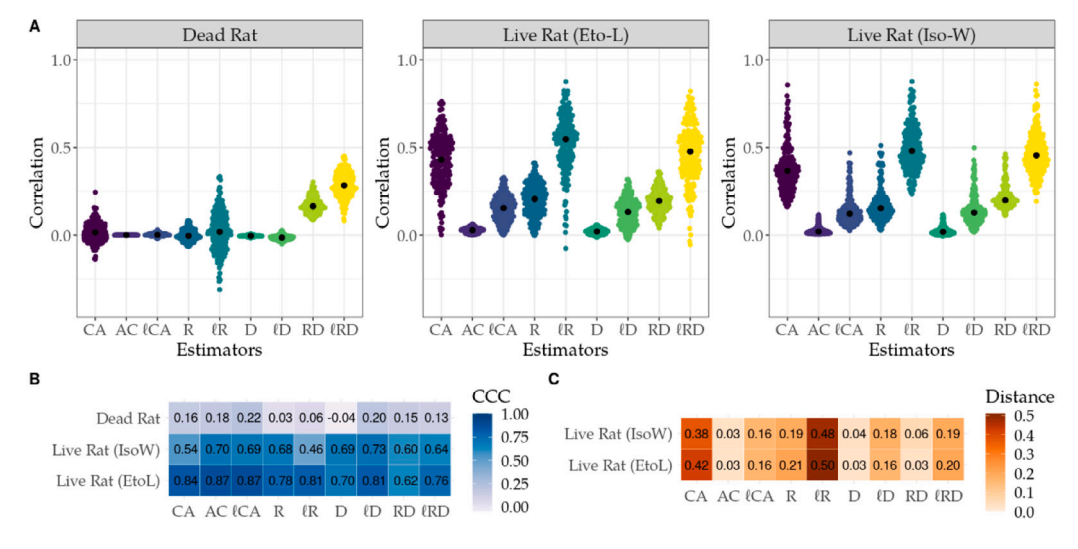


Fig. 6. Rat data results. A. Empirical distribution of the correlation estimators for all pairs of brain regions for a dead and two anesthetized rats, for all proposed estimators. In the dead rat, the correlation of averages (CA) estimator is providing high values where null correlations should be observed. For the live rat the average of correlation estimator (AC) is providing very low values where non null correlations should be observed. B. The Concordance Correlation Coefficient (CCC) for the repeatability of the different estimators for all rats, calculated between the first and second half of the BOLD time series. Higher CCC corresponds to a more repeatable estimator. C. Wasserstein distances between the correlation distribution of each anesthetized rat and that of the dead rat, for all estimators. AC, D, RD have a very low distance, indicating that correlation values are similar between dead and live rats for these estimators.

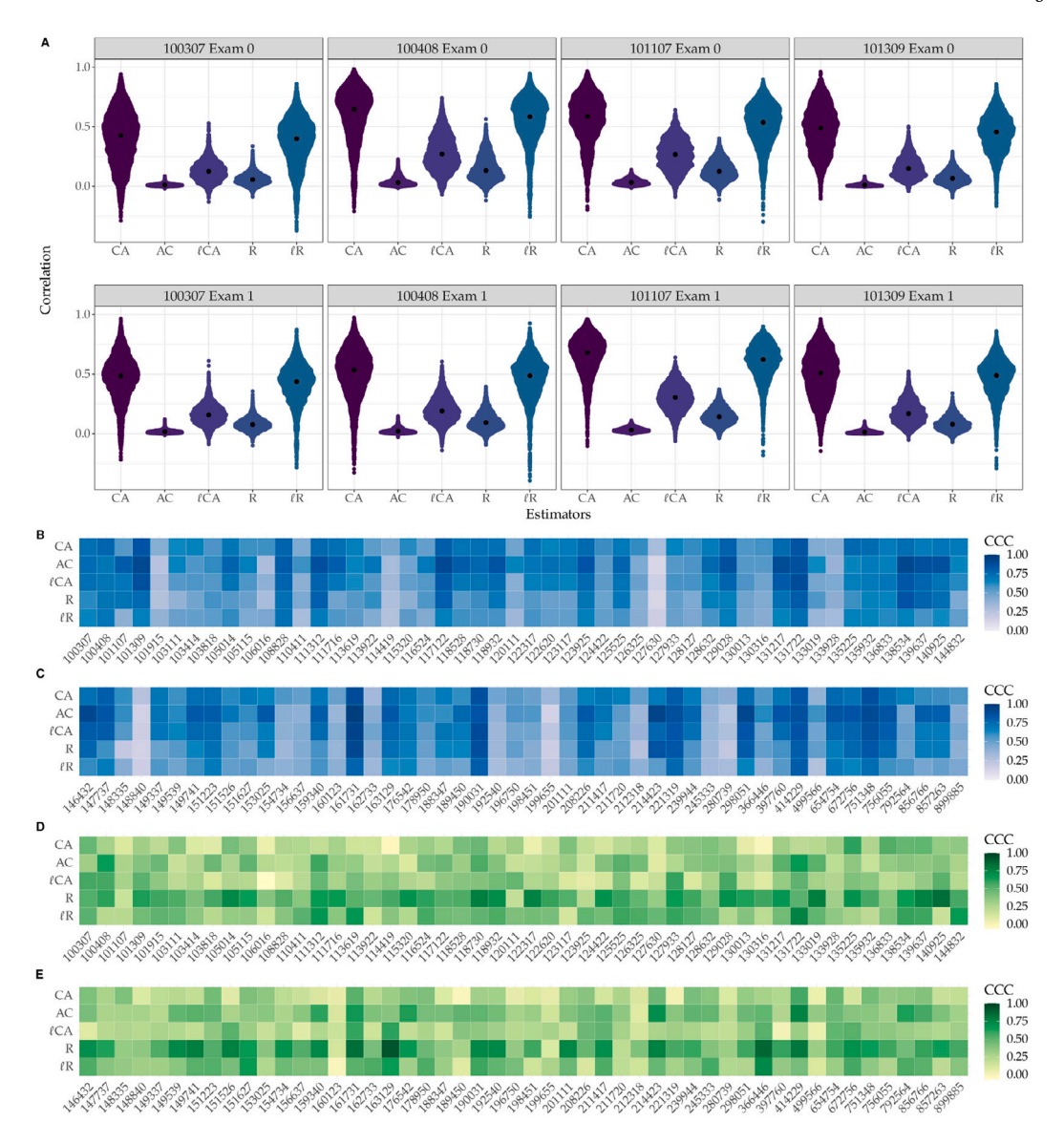


Fig. 7. Human data results. A. Empirical distribution of inter-regional correlations for three selected estimators for all pairs of brain regions for four human subjects. Each subject was scanned twice, on different days. B. and C. Concordance correlation Coefficient (CCC) for the reproducibility of the inter-regional correlation values obtained by different estimators for all human subjects, computed between the two examinations. Higher CCC indicates a more repeatable estimator. All estimators have broadly similar reproducibility. D. and E. reproducibility of a topological graph metric (betweenness). Again all estimators give broadly similar results, with slightly higher reproducibility for Ac.

We then quantified the edges in common between the networks obtained via the two estimators  $_{\text{CA}}$  (which is currently the most widely used estimator) and  $\ell_{\text{CA}}$ . For the dead rat, 67% of edges are in common between the two estimators. Additionally, 60% and 77% of edges are similar for the live rats.

# 6.3. Evaluation on human data

Based on our findings on the rats datasets, we evaluate the performances of the three estimators  $c_A$  (most common estimator, highest dead-live rat distance), AC (low dead-live rat distance) and  $\ell CA$  (high dead-live rat distance) for 100 subjects of the HCP dataset.

Fig. 7(A) reports the correlation values among all pairs of regions for four randomly selected HCP subjects. Consistent with the rat results, the estimator  $_{CA}$  yields the largest values of correlations, estimator  $_{AC}$  yields very low values, while  $_{CA}$  values are different from zero, but smaller that  $_{CA}$  values.

Reproducibility results for correlation estimates are shown in Fig. 7(B,C). The Concordance Correlation Coefficient was similar between estimators (average (sd) across 100 subjects for ca: 0.64 (0.13), ac: 0.66 (0.20),  $\ell$ ca: 0.62 (0.17), R: 0.56 (0.17),  $\ell$ R: 0.52 (0.14)), with variations in reproducibility reflecting inter-subject variability more than differences between estimators. For graph metrics reproducibility, we report only the results with betweenness in Fig. 7(D,E), since similar results are obtained with other metrics. Here, the methods differed more, with average (sd) across 100 subjects for ca: 0.29 (0.14), ac: 0.55 (0.17),  $\ell$ ca: 0.4 (0.16), R: 0.37 (0.14),  $\ell$ R: 0.26 (0.15).  $\ell$ ca had significantly lower CCC than ac (T = -6.8, p = 1.6 $e^{-10}$ ), However,  $\ell$ ca has significantly higher CCC than ca (T = 5.1, p = 8 $e^{-07}$ ) and  $\ell$ R (T = 6.3, p = 2 $e^{-9}$ ). Finally  $\ell$ ca and R are not significantly different (T = 1.35, p = 0.18). These differences are robust to the choice of threshold (cf, Appendix G.5).

Fig. 8. Largest differences between the cA and  $\ell cA$  estimators, median over 100 HCP subjects. Only the top 20% differences are shown. Inter-regional correlations are taken in absolute value and rank-transformed prior to computing differences (rank 1 for the strongest correlation, rank 2 for the second-strongest, and so on). Red indicates absolute correlations that are higher for the  $\ell cA$  than the cA estimator, while blue indicates the reverse. Node size is proportional to region size in the atlas. Estimator cA on average shows hyperconnectivity in occipital and generally dorsal posterior regions, and hypoconnectivity in frontal, temporal, and general ventral anterior regions.

**Table 2**Discriminative power of estimators on the human dataset. intra: Within-subject average and standard deviation of graph distances between first and second imaging session across 100 subjects; inter: same for between-subjects, using only the first session. W: average one-sided Wilcoxon rank-sum test value on 10 random splits, with corresponding harmonic mean *p*-value.

Estimator	Intra (sd)	Inter (sd)	W (p-value)	Identification rate
CA	0.29 (0.10)	0.49 (0.10)	$-5.82 \ (p_{hmp} = 1.5e^{-10})$	72%
AC	0.19 (0.10)	0.32 (0.10)	$-4.88 \ (p_{hmp} = 3.6e^{-9})$	69%
$\ell$ CA	0.26 (0.10)	0.43 (0.10)	$-3.315.58 (p_{hmp} = 1.2e^{-9})$	72%

In the thresholded graphs, the percentage of edges in common between estimators  $c_A$  and  $\ell c_A$  was on average equal to 70% for the one hundred subjects used in this analysis for both sessions. Fig. 8 shows median differences between the estimators in brain space across the HCP subjects.

Looking at dependence on region size, the CA estimator showed significantly more correlation with region size than the  $\ell$ CA estimator (average (sd) across 100 subjects 0.55 (0.10) vs. 0.40 (0.09), T = 27.2,  $p = 1.1e^{-47}$ ).

In terms of discriminative power between subjects, for connectome fingerprinting,  $c_A$  and  $\ell'c_A$  achieved the same performance (72% correct identification), while  $a_C$  had slightly lower performance (68% correct identification). Group differences were also similar between estimators. Table 2 provides details.

# 7. Discussion

In this paper we illustrate the effect of averaged data on estimators of correlation when two types of noises are present, local and global noise. The use of the classical correlation of averages is hindered by the presence of these noises in addition to the presence of intracorrelations. We proposed alternative estimators including correction terms to compensate the intra-correlations, local and global noises. The performance of these estimators was evaluated on simulations, rats data, and human data, yielding several observations.

#### 7.1. The correlation of averages estimator is highly biased

The CA estimator tends to be highly biased, as illustrated on synthetic data where the ground truth is known, but also compared to other estimators, as shown on live rats and human data, where the mode of the distribution of correlation values is systematically among the highest found. We hypothesize that this is driven by a combination of low intra-correlation and large region sizes, which further lowers intra-correlation. This can be seen from the estimator definition in Eq. (4). We also note that the  $\ell$ CA estimator effectively reduces this influence of region size.

In addition, Fig. 8 revealed a systematic spatial bias between the  $_{\text{CA}}$  and  $_{\text{CA}}$  estimator, exhibiting dorsal posterior hyper-connectivity for

ca, and corresponding ventral anterior hypo-connectivity. The figure also suggests that the largest differences between the two estimators appear between regions that are the largest, further highlighting the reduced dependency to region size for the  $\ell_{CA}$  estimator. The spatial distribution of these differences suggests that caution is in order when examining large-scale resting-state networks derived from the CA estimator, as some apparent topological properties of brain networks, such as modularity, could be driven in part by region size and region intracorrelation. Indeed, in our experiments, thresholded graphs differed in a large proportion of edges, both in rats (around 30%-50% edge differences) and humans (around 30% edge differences). Thus, it is probable that both edge-level and graph-level metrics obtained from the CA estimator are biased due to their over- or under-estimation of actual functional connectivity, in a spatially-dependent manner. For clinical applications, this phenomenon could either emphasize or reduce differences between patients and controls. Since we have no ground truth available for in-vivo functional connectivity, in practical situations, we therefore recommend that results obtained with the CA estimator be re-run at least with the  $\ell$ CA estimator as a sensitivity analysis. The computational cost is not excessive, and differences in results could indicate that estimator-induced bias was at play.

# 7.2. Local noise and intra-correlation link to long-range correlation

In this paper, we explain the bias observed in ca estimator by introducing hypotheses on both intra-correlation and noise. Indeed, previous studies on regional homogeneity (Zang et al., 2004) showed relevant results on classification of pathologies based only on intra-regional properties. This was confirmed by a recent work on classification of intra-correlation (Petersen et al., 2016) using Wasserstein distances. Based on these findings, we hypothesize that bias observed on intercorrelation is driven by intra-correlation and noise. Our simple simulation model illustrates the effect of local noise and intra-correlation. This is clearly displayed in Figs. 4–5, where the boxplots for the various estimators are plotted. However, it is important to note that under local noise, in this framework with controlled intra-correlation, estimator ca is relatively close to the exact value. This may be explained by a trade-off in the denominator of the limit as expressed in Table 1. In our simulation, we also observed that the ca estimators bias depends

on the intra-correlation and local noise. Indeed, high values of CA tends to be observed when low values of intra-correlation are observed. These low values of intra-correlation have already been mentioned in the study of dynamics of neural networks (Deco et al., 2014) where local decorrelation was reported in real datasets. In our paper, for the first time, we proved a statistical explanation of the link between local decorrelations and long-range correlations using aggregated time series.

The model chosen in this paper for intra-correlation and local noise was driven by statistical motivations to be able to write explicit formulas for the limit of the estimators. However, as observed in Jiang and Zuo (2016) and Deco et al. (2014), these hypotheses are realistic for resting-state fMRI data, where local decorrelations are observed. These local decorrelations can come from two factors: a low intra-correlation (as modeled by the choice of the intra-correlation coefficients of the matrix), or a strong local noise. The stationarity assumption may be not adequate based on raw data. However, as mentioned in Section 2.1, it becomes very reasonable after performing a wavelet transform of each time series voxelwise. This preprocessing significantly reduces non stationary artefacts.

#### 7.3. Repeatability and reproducibility

Repeatability of correlation values in dead rats was very low for all estimators, consistent with the random nature of the data. For live rats, the CCC ranged from 0.46 to 0.87 depending on specimen and estimator. For humans, ca and  $\ell$ ca showed approximately the same reproducibility (0.63 average (0.2)), and ac was slightly superior (0.66 average (0.2)). But reproducibility differences between estimators were much less pronounced than reproducibility differences between individual subjects.

As a representative for the reproducibility of graph metrics, we investigated betweenness. Here, AC offered the highest reproducibility (average (sd): 0.55 (0.17)) and &CA improved markedly over CA (0.4 (0.16) vs. 0.29 (0.14)). This is contrast to another study that found no effect of aggregation method (region mean time series versus region median versus 1st eigenvariate of the region) on the reproducibility of graph metrics (Braun et al., 2012) (although in that study sessions were weeks apart).

## 7.4. Discriminability

Estimators  $CA, AC, \ell CA$  showed similar values for discriminability, with slightly lower identification rate and intra-subject to inter-subject distribution separation for AC than the two others, and slightly lower intra-inter separation for  $\ell CA$  than CA. This suggests that the improved robustness to region size and intra-correlation effects of  $\ell CA$  does not result in a sizeable impact on discriminative ability, although this warrants further evaluation.

#### 7.5. Limitations

Our signal model, and therefore the derived estimators, is a tradeoff between model realism and tractability of the analysis of estimator properties. This comes with important limitations.

First, assuming stationarity and additivity of the local noise fails to capture effects like system instability due to B0 inhomogeneity, RF power variations, or gradient fluctuations (Lazar, 2008; Greve et al., 2013; Liu, 2016). Independently of the model, note that effects such as drift are mitigated by using wavelet coefficient time series as we did in this study, and that such instabilities explain proportionally less of the noise variance than thermal noise at high field (Greve et al., 2011).

Second, motion effects, and in particular differential long-vs. short-range effects on correlations (Van Dijk et al., 2010; Yan et al., 2013), were not studied, and their interplay with the spatial bias exhibited by estimator CA in Fig. 8 was not examined.

Third, our new estimators come with the added burden of choosing hyperparameters such as neighborhood size. These are currently selected empirically, and no systematic sensitivity analysis has been performed. However, our proposed approach may be used to redefine the brain regions by grouping voxels with high intra-correlation. This would allow to define new brain regions using intra-correlation in addition to anatomical criterion.

Despite these limitations, we believe our empirical tests served to bridge the gap towards applicability, since our model yielded at least an estimator,  $\ell_{CA}$ , with useful properties for use in neuroimaging — namely, reduced dependency to region size and low intra-correlation, and improved reproducibility of graph metrics.

#### CRediT authorship contribution statement

Sophie Achard: Conceptualization, Methodology, Software, Visualisation, Writing – review & editing. Jean-François Coeurjolly: Conceptualization, Methodology, Software, Visualisation, Writing – review & editing. Pierre Lafaye de Micheaux: Conceptualization, Methodology, Software, Visualisation, Writing – review & editing. Hanâ Lbath: Conceptualization, Methodology, Software, Visualisation, Writing – review & editing. Jonas Richiardi: Conceptualization, Methodology, Software, Visualisation, Writing – review & editing.

#### Declaration of competing interest

The authors declare that they have no known competing financial interests or personal relationships that could have appeared to influence the work reported in this paper.

#### Data availability

See Section 5 for details of data and code availability

#### Acknowledgments

This work was partly funded by French National Research Agency project ANR-20-NEUC-0003-02. Rat data was acquired at the IRMaGe MRI facility, partly funded by the French program Investissement d'Avenir run by the French National Research Agency, grant Infrastructure d'avenir en Biologie Santé ANR-11-INBS-0006. The work was also partly funded by the transnational Alliance Campus Rhodanien programme. Human data were provided by the Human Connectome Project, WU-Minn Consortium (Principal Investigators: David Van Essen and Kamil Ugurbil; 1U54MH091657) funded by the 16 NIH Institutes and Centers that support the NIH Blueprint for Neuroscience Research; and by the McDonnell Center for Systems Neuroscience at Washington University. We also thank Ayoub Cherkaoui and Ossama Ziri for coding the Python implementation of the estimators.

# Appendix A. Brain functional connectivity review

The literature review was conducted on PubMed using the keywords "brain connectivity graph resting state 'human connectome project" on September 30, 2021. The search returned 32 papers written between 2014 and 2021. Out of those papers, 5 were not open access and 2 papers were literature reviews, and were not considered further. 3 papers were either using seed-based or voxel-to-voxel correlation. Out of the remaining 24 papers 71% (17/24) first averaged voxels before computing the inter-regional correlations and 88% (21/24) employed some kind of spatial aggregation method, including but not limited to averaging over voxels, ICA or dictionary learning.

#### Appendix B. Hypotheses for the spatio-temporal model

The assumptions on the model can be written as follows. For any  $i, i' \in C$  and s, t = 1, ..., T,

$$\begin{split} & \mathrm{E}[X_i(t)] = \mathrm{E}[\varepsilon_i(t)] = \mathrm{E}[e(t)] = 0, \\ & \mathrm{E}[X_i(s)X_i(t)] = \mathrm{E}[\varepsilon_i(s)\varepsilon_i(t)] = E[e(s)e(t)] = 0, \\ & \mathrm{E}[X_i(s)\varepsilon_{i'}(t)] = \mathrm{E}[X_i(s)e(t)] = \mathrm{E}[\varepsilon_i(s)e(t)] = 0, \\ & \mathrm{E}[e(t)^2] = \sigma_*^2. \end{split}$$

Let  $\Sigma$  be the covariance matrix of the vector  $(Y_i(t))_{i \in C, t=1, \ldots, T}$ . In this paper, we assume without referring specifically to this assumption that the parameters  $\sigma_j^2$ ,  $\sigma_\epsilon^2$ ,  $\sigma_e^2$ ,  $\rho_{ii'}$ ,  $\eta_{ii'}$ ,  $r_{jj'}$  are such that  $\Sigma$  is a positive definite matrix.

We also assume that the random variables are independent in time. This is not overly restrictive: in particular, if the random variables have long memory, after a wavelet decomposition, the random variables can be approximated to be decorrelated in time for large wavelet scales (Moulines et al., 2007). In addition, assuming that the  $X_i$ 's are centered is coherent as it is a well-known fact that a wavelet decomposition based on a wavelet mother with K vanishing moments cancels out every polynomial trend with degree K-1.

Finally, to apply the law of large numbers, we also assume that all random variables are absolutely integrable, that is  $E[|Z_i(t)|] < \infty$  for  $Z = X, \varepsilon, e, i \in C$  and t = 1, ..., T.

#### Appendix C. Properties of the estimators of interest

For any set of indices E with cardinality #E, we let

$$\bar{\rho}_E = \frac{1}{(\#E)^2} \sum_{i,i' \in E} \rho_{ii'}$$
 and  $\bar{\eta}_E = \frac{1}{(\#E)^2} \sum_{i,i' \in E} \eta_{ii'}$ . (C.1)

The results of the paper are based on this proposition:

**Proposition C.1.** Consider the notation of Section 2.1 and assumptions described in Appendix B. Let  $j, j' \in \{1, ..., J\}$ .

(i) Let 
$$E \subseteq \mathcal{R}_i$$
, then for any  $t = 1, ..., T$ 

$$Var[\bar{X}_E(t)] = \sigma_i^2 \,\bar{\rho}_E \tag{C.2}$$

$$\operatorname{Var}[\bar{\varepsilon}_{E}(t)] = \sigma_{\varepsilon}^{2} \,\bar{\eta}_{E} = \mathcal{O}(1/(\#E)) \tag{C.3}$$

$$Var[\bar{e}_E(t)] = Var(e(t)) = \sigma_e^2$$
 (C.4)

$$\operatorname{Var}[\bar{Y}_{E}(t)] = \sigma_{i}^{2} \bar{\rho}_{E} + \sigma_{\varepsilon}^{2} \bar{\eta}_{E} + \sigma_{e}^{2}. \tag{C.5}$$

(ii) Let  $E \subseteq \mathcal{R}_i$  and  $E' \subseteq \mathcal{R}_{i'}$ , then

$$\operatorname{Cov}[\bar{Y}_{E}(t), \bar{Y}_{E'}(t)] = \begin{cases} \sigma_{j}\sigma_{j'}r_{jj'} + \sigma_{e}^{2} & \text{if } j \neq j' \\ \sigma_{j}^{2}\bar{\rho}_{E,E'} + \sigma_{e}^{2} & \text{if } j = j' \end{cases}$$
(C.6)

where

$$\bar{\rho}_{E,E'} = \frac{1}{(\#E)(\#E')} \sum_{i \in E, i' \in E'} \rho_{|i-i'|}.$$
 (C.7)

(iii) Let  $i \in E \subseteq \mathcal{R}_j$  and  $i' \in E' \subseteq \mathcal{R}_{j'}$  and assume for any  $i \in E$  and  $i' \in E' |i-i'| \ge p$  (in the case j=j'). Then as  $T \to \infty$ , the following statements hold almost surely.

$$\widehat{\sigma}^{2}(\mathbf{Y}_{i}) \overset{a.s.}{\to} \operatorname{Var}[Y_{i}(1)] \qquad and \qquad \widehat{\operatorname{Cov}}[\mathbf{Y}_{i}, \mathbf{Y}_{i'}] \overset{a.s.}{\to} \operatorname{Cov}[Y_{i}(1), Y_{i'}(1)] \quad \text{(C.8)}$$

$$\widehat{\sigma}^{2}(\bar{\mathbf{Y}}_{E}) \overset{a.s.}{\to} \operatorname{Var}[\bar{Y}_{E}(1)] \qquad and \qquad \widehat{\operatorname{Cov}}[\bar{\mathbf{Y}}_{E}, \bar{\mathbf{Y}}_{E'}] \overset{a.s.}{\to} \operatorname{Cov}[\bar{Y}_{E}(1), \bar{Y}_{E'}(1)].$$

Proposition C.1 is given without proof. (i)–(ii) ensue from the model (1) while (iii) is quite straightforward since we have assumed independence in time.

As seen from Proposition C.1, the quantity  $\bar{\eta}_E$  is related to the correlation structure of the local noise. By assuming this noise to be p-dependent (that is  $\eta_\delta=0$  when  $\delta\geq p$ ), it is clear that the larger #E the smaller  $\bar{\eta}_E$ .

#### Appendix D. Consistency results for the existing estimators

D.1. Consistency of  $\hat{r}_{ii'}^{CA}$ 

Proposition C.1 shows  $\hat{r}^{c_{\Lambda}}_{jj'}$  is a strongly consistent estimator of  $r^{c_{\Lambda}}_{jj'}$  as  $T \to \infty$  where

$$r_{jj'}^{\text{CA}} = r_{jj'} \frac{1 + \sigma_{e,jj'}^2 / r_{jj'}}{\sqrt{(\bar{\rho}_{R_j} + \sigma_{e,j}^2 \bar{\eta}_{R_j} + \sigma_{e,j}^2)(\bar{\rho}_{R_{j'}} + \sigma_{e,j'}^2 \bar{\eta}_{R_{j'}} + \sigma_{e,j'}^2)}}.$$
 (D.1)

Another way to correct the size effect is to compensate the intercorrelation by the intra-correlation. This would lead to the following estimator:

$$\widehat{r}_{jj'}^{\widetilde{\text{AC}}} = \frac{1}{N_j N_{j'}} \left( \sum_{i,i' \in \mathcal{R}_j} \widehat{\text{Cor}}(\mathbf{Y}_i, \mathbf{Y}_{i'}) \sum_{i,i' \in \mathcal{R}_{j'}} \widehat{\text{Cor}}(\mathbf{Y}_i, \mathbf{Y}_{i'}) \right)^{1/2} \widehat{r}^{\text{AC}}.$$
(D.2)

The two estimators (5) and (D.2) have the important property to remove the size effect (since when  $\sigma_{\varepsilon}=\sigma_{e}=0$ ,  $r_{jj'}^{{\scriptscriptstyle AC}}=r_{jj'}$ ). Note that both estimators tend to the same limit.

D.2. Consistency of  $\hat{r}_{ii'}^{AC}$ 

Proposition C.1 shows that  $\hat{r}^{\rm AC}_{jj'}$  is a strongly consistent estimator of  $r^{\rm AC}_{ij'}$  given by

$$r_{jj'}^{\text{AC}} = r_{jj'} \frac{1 + \sigma_{e,jj'}^2 / r_{jj'}}{\sqrt{(1 + \sigma_{e,j}^2 + \sigma_{e,j}^2)(1 + \sigma_{e,i'}^2 + \sigma_{e,j'}^2)}}.$$
 (D.3)

As revealed by (D.1) and (D.3),  $\hat{r}_{jj'}^{\text{CA}}$  and  $\hat{r}_{jj'}^{\text{AC}}$  do not converge towards  $r_{jj'}$  when a local noise or global noise is present. We could ask why  $\hat{r}_{jj'}^{\text{CA}}$  is interesting. Actually, a first spatial averaging tends to decrease the effect of the local noise. Indeed, when  $\sigma_e^2 = 0$  (and with equal unit variances to simplify), we have

$$r_{jj'}^{\scriptscriptstyle{\mathrm{CA}}} = \frac{r_{jj'}}{\sqrt{(\bar{\rho}_{R_j} + \sigma_{\varepsilon}^2 \bar{\eta}_{R_j})(\bar{\rho}_{R_{j'}} + \sigma_{\varepsilon}^2 \bar{\eta}_{R_{j'}})}} \quad \text{ and } \quad r_{jj'}^{\scriptscriptstyle{\mathrm{AC}}} = \frac{r_{jj'}}{1 + \sigma_{\varepsilon}^2}.$$

Hence, if we expect that  $\bar{\rho}_{\mathcal{R}_j} \approx \bar{\rho}_{\mathcal{R}_{j'}} \approx 1$ ,  $\hat{r}_{jj'}^{\text{cA}}$  will be a better estimator since  $\bar{\eta}_{\mathcal{R}_j} = \mathcal{O}(1/N_j)$ . A natural compromise between  $\hat{r}_{jj'}^{\text{cA}}$  and  $\hat{r}_{jj'}^{\text{cA}}$  can be defined using local neighborhood as defined by  $\ell$ ca.

D.3. Consistency of  $\hat{r}_{ij}^{R}$ 

From Proposition C.1, as  $T \to \infty$ 

$$\frac{1}{4} \sum_{\alpha,\beta=1}^{2} \widehat{\mathrm{Cor}}(\mathbf{Y}_{i_{\alpha}^{(b)}}, \mathbf{Y}_{i_{\beta}^{\prime(b)}}) \overset{a.s.}{\rightarrow} \frac{\sigma_{j} \sigma_{j'} r_{jj'} + \sigma_{e}^{2}}{\sqrt{\left(\sigma_{j}^{2} + \sigma_{\varepsilon}^{2} + \sigma_{e}^{2}\right) \left(\sigma_{j'}^{2} + \sigma_{\varepsilon}^{2} + \sigma_{e}^{2}\right)}}$$

and

$$\widehat{\operatorname{Cor}}(\mathbf{Y}_{i_{1}^{(b)}}, \mathbf{Y}_{i_{2}^{(b)}}) \stackrel{a.s.}{\to} \frac{\sigma_{j}^{2} \rho_{\delta} + \sigma_{e}^{2}}{\sigma_{i}^{2} + \sigma_{e}^{2} + \sigma_{e}^{2}},$$

whereby we deduce that  $\hat{r}^R$  is a strongly consistent estimator of

$$r_{jj'}^{\rm R} = r_{jj'} \frac{1 + \sigma_{e,jj'}^2 / r_{jj'}}{\sqrt{|(\rho_{\delta} + \sigma_{e,j}^2)(\rho_{\delta} + \sigma_{e,j'}^2)|}}.$$
 (D.4)

From (D.4), we observe that when  $\sigma_e=0$  then for any unknown value of  $\sigma_{\epsilon}$ ,  $\hat{r}_{jj'}^{R}$  estimates consistently  $r_{jj'}/|\rho_{\delta}|$  which should be close to  $r_{jj'}$  if we take  $\delta=p$  and expect that  $\rho_p$  is close to 1. In other words, the estimator  $\hat{r}_{jj'}^{R}$  is robust to the size of the regions and robust to a possible local noise

To reduce the assumption that  $\rho_p$  is close to 1, we can combine this idea of replicates with local averaging. This is the topic of the next section.

(C.9)

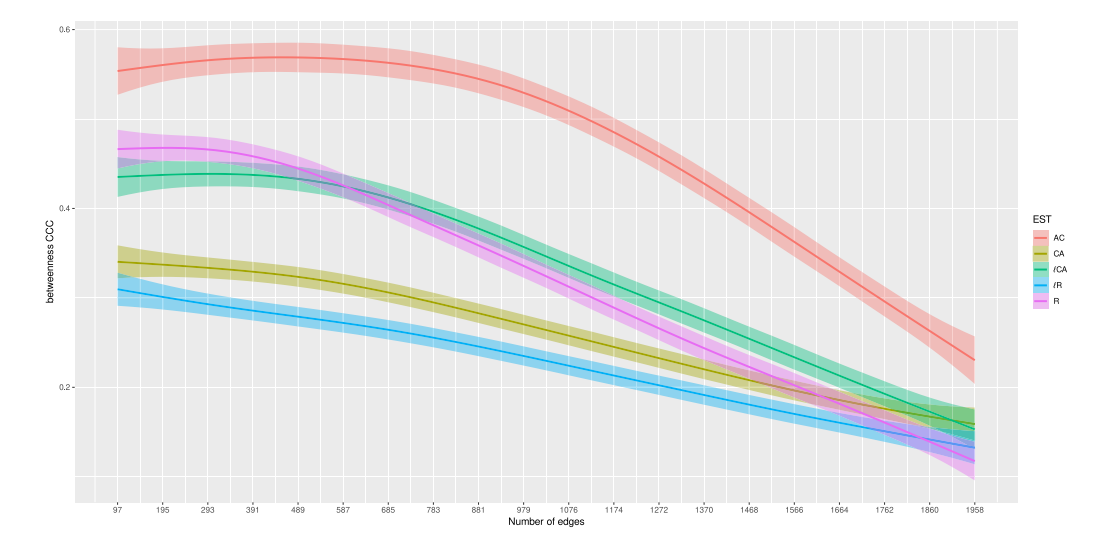


Fig. G.9. CCC of betweenness according to different choices of threshold and for the different estimators.

# Appendix E. Consistency of $\hat{r}^{\mathrm{D}}_{\cdot\cdot}$

The following result is the key ingredient:

**Proposition E.1.** Under the notation of this section, as  $T \to \infty$ , the following statements hold almost surely.

$$\widehat{\mathrm{Cov}}(\mathbf{Y}_{i^{(b)}} - \mathbf{Y}_{k^{(b)}}, \mathbf{Y}_{i'^{(b)}} - \mathbf{Y}_{k'^{(b)}}) \stackrel{a.s.}{\to} \sigma_i \sigma_{i'} r_{ii'}.$$

$$2\hat{s}^2(\mathbf{Y}_{i^{(b)}}, \mathbf{Y}_{k^{(b)}}, \mathbf{Y}_{k^{\prime(b)}}) \stackrel{a.s.}{\to} 2\sigma_j^2 + 2\sigma_{\varepsilon}^2. \tag{E.1}$$

Proof. (i) Using the independence in time, it is clear that the lefthand side converges almost surely to  $Cov(Y_{i(b)}(1) - Y_{k(b)}(1), Y_{i'(b)}(1) - Y_{k(b)}(1))$  $Y_{k'(b)}(1) = \sigma_j \sigma_{j'} r_{jj'} + \sigma_e^2 - 2\sigma_e^2 + \sigma_e^2$  since the two regions  $\mathcal{R}_k$  and  $\mathcal{R}_{k'}$ are disconnected, which leads to the result.

(ii) In the same way, the left-hand side tends to  $Var(Y_{i^{(b)}}(1)-Y_{k^{(b)}}(1))+$  $\operatorname{Var}(Y_{i^{(b)}}(1) - Y_{k'^{(b)}}(1)) - \operatorname{Var}(Y_{k^{(b)}}(1) - Y_{k'^{(b)}}(1)) = \sigma_j^2 + \sigma_k^2 + \sigma_{k'}^2 + 4\sigma_{\varepsilon}^2 - \sigma_k^2 - \sigma_{k'}^2 + \sigma_{k'}^2$  $\sigma_{k'}^2 - 2\sigma_{\varepsilon}^2$  which yields the stated limit.  $\square$ 

In other words, Proposition E.1 shows that  $\hat{r}_{ii'}^{D}$  is a strongly consistent estimator of  $r_{ii'}^{D}$  given by

$$r^{\mathrm{D}} = r_{jj'} \frac{1}{\sqrt{\left(1 + \sigma_{\varepsilon,j}^2\right) \left(1 + \sigma_{\varepsilon,j'}^2\right)}}$$
(E.2)

which, in the situation where  $\sigma_{\varepsilon} = 0$ , is nothing else than  $r_{ii'}$ .

# Appendix F. Consistency of $\hat{r}_{::i}^{RD}$

The following result is a consequence of Propositions C.1–G.1.

**Proposition F.1.** As  $T \to \infty$ , the following statements hold almost surely. (i) For any  $i_1, i_2 \in \mathcal{R}_j$ ,  $i'_1, i'_2 \in \mathcal{R}_j$   $i_k \in \mathcal{R}_k$  and  $i_{k'} \in \mathcal{R}_{k'}$ , such that  $|i_2 - i_1| = |i_2' - i_1'| = \delta \ge p$ 

$$\sqrt{|\widetilde{\operatorname{Cor}}(\mathbf{Y}_{i_1},\mathbf{Y}_{i_2};\mathbf{Y}_{i_k},\mathbf{Y}_{i_{k'}})\widetilde{\operatorname{Cor}}(\mathbf{Y}_{i'_1},\mathbf{Y}_{i'_2};\mathbf{Y}_{i_k},\mathbf{Y}_{i_{k'}})|} \overset{a.s.}{\to} \frac{\sigma_j\sigma_{j'}|\rho_{\delta}|}{\sqrt{(\sigma_j^2+\sigma_{\varepsilon}^2)(\sigma_{j'}^2+\sigma_{\varepsilon}^2)}} \qquad r_{jj'}^{\ell \mathbb{R}} = r_{jj'} \quad \frac{1+\sigma_{e,jj'}^2/r_{jj'}}{\sqrt{|(\bar{\rho}_{\mathcal{V},\mathcal{V}',\delta}+\sigma_{e,j}^2)(\bar{\rho}_{\mathcal{V},\mathcal{V}',\delta}+\sigma_{e,j'}^2)|}}$$
where  $\bar{\rho}_{\mathcal{V},\mathcal{V}',\delta}$  is defined by (C.7) with  $\mathcal{V}$  and

(ii) For any v-neighborhoods  $V_{j_1}, V_{j_2} \in \mathcal{R}_j$ ,  $V_{j'_1}, V_{j'_2} \in \mathcal{R}_{j'}$   $V_k \in \mathcal{R}_k$  $\mathcal{V}_{k'} \in \mathcal{R}_{k'}$ , such that for any  $i_1 \in \mathcal{V}_{j_1}$ ,  $i_2 \in \mathcal{V}_{j_2}$ ,  $i'_1 \in \mathcal{V}'_{j_1}$ ,  $i'_2 \in \mathcal{V}'_{j_2}$ 

$$|i_1 - i_2| = |i'_1 - i'_2| = \delta \ge p$$

$$\begin{split} |\widetilde{\operatorname{Cor}}(\bar{\mathbf{Y}}_{\mathcal{V}_{j_{1}}}, \bar{\mathbf{Y}}_{\mathcal{V}_{j_{2}}}; \bar{\mathbf{Y}}_{\mathcal{V}_{k}}, \bar{\mathbf{Y}}_{\mathcal{V}_{k'}}) \widetilde{\operatorname{Cor}}(\bar{\mathbf{Y}}_{\mathcal{V}_{j'_{1}}}, \bar{\mathbf{Y}}_{\mathcal{V}_{j'_{2}}}; \bar{\mathbf{Y}}_{\mathcal{V}_{k}}, \bar{\mathbf{Y}}_{\mathcal{V}_{k'}})| \stackrel{a.s.}{\to} \\ \frac{\sigma_{j}^{2} \sigma_{j'}^{2} \rho_{\mathcal{V}, \mathcal{V}'}^{2}, \delta}{(\sigma_{j}^{2} \bar{\rho}_{\mathcal{V}} + \sigma_{\varepsilon}^{2} \bar{\eta}_{\mathcal{V}})(\sigma_{j'}^{2} \bar{\rho}_{\mathcal{V}} + \sigma_{\varepsilon}^{2} \bar{\eta}_{\mathcal{V}})} \end{split}$$
(F.2)

where V, V' are two v-neighborhoods at distance  $\delta$ .

Propositions G.1-F.1 show that  $\hat{r}_{ii'}^{RD}$  is a strongly consistent estimator of  $r_{ii'}^{RD}$  given by

$$r_{jj'}^{\text{RD}} = \frac{r_{jj'}}{|\rho_s|} \tag{F.3}$$

# Appendix G. Consistency of localized versions of estimators

G.1. Consistency of  $\hat{r}_{ii'}^{\ell CA}$ 

We can apply Proposition C.1 to show that  $r_{ii'}^{\ell_{CA}}$  is a strongly consistent estimator of

$$r_{jj'}^{\ell_{\text{CA}}} = r_{jj'} \frac{1 + \sigma_{e,jj'}^2 / r_{jj'}}{\sqrt{(\bar{\rho}_{\mathcal{V}} + \sigma_{e,j}^2 \bar{\eta}_{\mathcal{V}} + \sigma_{e,j'}^2)(\bar{\rho}_{\mathcal{V}} + \sigma_{e,j'}^2 \bar{\eta}_{\mathcal{V}} + \sigma_{e,j'}^2)}}$$
(G.1)

where V is any v-neighborhood. When there is no global noise ( $\sigma_e = 0$ ) and for moderate  $\nu$ , it may be expected than the denominator of  $r_{ii'}^{\ell c_A}$ is closer to 1 than the ones of  $r_{ii'}^{CA}$  and  $r_{ii'}^{AC}$ .

# G.2. Consistency of $\hat{r}_{ii'}^{\ell R}$

Proposition C.1 shows that  $\hat{r}_{ij'}^{\ell \mathrm{R}}$  is a strongly consistent estimator of  $r_{ii'}^{\ell R}$  defined by

$$r_{jj'}^{\ell R} = r_{jj'} \frac{1 + \sigma_{e,jj'}^2 / r_{jj'}}{\sqrt{|(\bar{\rho}_{\mathcal{V},\mathcal{V}',\delta} + \sigma_{e,j}^2)(\bar{\rho}_{\mathcal{V},\mathcal{V}',\delta} + \sigma_{e,j'}^2)|}}$$
(G.2)

where  $\bar{\rho}_{\mathcal{V},\mathcal{V}',\delta}$  is defined by (C.7) with  $\mathcal{V}$  and  $\mathcal{V}'$  two  $\nu$ -neighborhoods at distance  $\delta$ . Similarly to the estimator  $\hat{r}^{R}$ , when  $\sigma_{e} = 0$ , the previous expression reduces to  $r_{jj'}^{\ell R}=r_{jj'}/|\bar{\rho}_{\mathcal{V},\mathcal{V}',\delta}|$  and again it is not unreasonable to think that  $\bar{\rho}_{\mathcal{V},\mathcal{V}',\delta}$  is close to 1.

# G.3. Consistency of $\hat{r}_{ii'}^{\ell D}$

The following result is an adaptation of Proposition E.1 to local averages.

**Proposition G.1.** As  $T \to \infty$ , the following statements hold almost surely.

$$\widehat{\mathrm{Cov}}(\bar{\mathbf{Y}}_{\mathcal{V}_{j}^{(b)}} - \bar{\mathbf{Y}}_{\mathcal{V}_{k}^{(b)}}, \bar{\mathbf{Y}}_{\mathcal{V}_{j'}^{(b)}} - \bar{\mathbf{Y}}_{\mathcal{V}_{k'}^{(b)}}) \overset{a.s.}{\rightarrow} \sigma_{j}\sigma_{j'}r_{jj'}.$$

(ii)

$$2\hat{s}^2(\bar{\mathbf{Y}}_{\mathcal{V}_{i}^{(b)}}, \bar{\mathbf{Y}}_{\mathcal{V}_{i}^{(b)}}, \bar{\mathbf{Y}}_{\mathcal{V}_{i}^{(b)}}) \stackrel{a.s.}{\to} 2\sigma_j^2 \bar{\rho}_{\mathcal{V}} + 2\sigma_{\varepsilon}^2 \bar{\eta}_{\mathcal{V}}. \tag{G.3}$$

Using Proposition G.1 (for which proof follows along similar lines as Proposition E.1), we deduce that  $\hat{r}_{jj'}^{\ell D}$  is a strongly consistent estimator of  $r_{ij'}^{\ell D}$  given by

$$r_{jj'}^{\ell \mathrm{D}} = r_{jj'} \ \frac{1}{\sqrt{(\bar{\rho}_{\mathcal{V}} + \sigma_{\varepsilon,j}^2 \bar{\eta}_{\mathcal{V}})(\bar{\rho}_{\mathcal{V}} + \sigma_{\varepsilon,j'}^2 \bar{\eta}_{\mathcal{V}})}} \tag{G.4}$$

where V is any v-neighborhood.

# G.4. Consistency of $\hat{r}_{ii'}^{\ell RD}$

Propositions G.1–F.1 show that  $\hat{r}_{jj'}^{\ell \text{RD}}$  is a strongly consistent estimator of  $r_{ii'}^{\ell \text{RD}}$  given by

$$r_{jj'}^{\ell RD} = \frac{r_{jj'}}{|\bar{\rho}_{\mathcal{V},\mathcal{V}',\delta}|} \tag{G.5}$$

where  $\mathcal{V}$  and  $\mathcal{V}'$  are two  $\nu$ -neighborhoods at distance  $\delta$ . Similarly to the previous estimator,  $\hat{r}_{ij'}^{\ell RD}$  is robust to an additive global and local noise.

#### G.5. Robustness of CCC differences in terms of threshold

In the main text, we presented the difference of CCC for the different estimators based on a single threshold corresponding to 20% of the edges of the graph. Fig. G.9 displays the variability of CCC according to different number of edges selected to construct the graph. This shows the robustness of our findings where  $\ell_{\text{CA}}$  has always higher CCC than ca for all possible thresholds.

#### References

- Achard, S., Coeurjolly, J.-F., Marcillaud, R., Richiardi, J., 2011. fMRI functional connectivity estimators robust to region size bias. In: IEEE Workshop on Statistical Signal Processing, SSP2011. Nice, France, pp. 813–816.
- Achard, S., Salvador, R., Whitcher, B., Suckling, J., Bullmore, E., 2006. A resilient, low-frequency, small-world human brain functional network with highly connected association cortical hubs. J. Neurosci. 26 (1), 63–72.
- Afyouni, S., Smith, S.M., Nichols, T.E., 2019. Effective degrees of freedom of the Pearson's correlation coefficient under autocorrelation. NeuroImage 199, 609–625.
- Alexander-Bloch, A.F., Gogtay, N., Meunier, D., Birn, R., Clasen, L., Lalonde, F., Lenroot, R., Giedd, J., Bullmore, E.T., 2010. Disrupted modularity and local connectivity of brain functional networks in childhood-onset schizophrenia. Front. Syst. Neurosci. 4.
- Alexander-Bloch, A.F., Shou, H., Liu, S., Satterthwaite, T.D., Glahn, D.C., Shi-nohara, R.T., Vandekar, S.N., Raznahan, A., 2018. On testing for spatial correspondence between maps of human brain structure and function. NeuroImage 178, 540–551.
- Becq, G.G.J.-P.C., Barbier, E., Achard, S., 2020a. Brain networks of rats under anesthesia using resting-state fMRI: comparison with dead rats, random noise and generative models of networks. J. Neural Eng..
- Becq, G.J.-P., Habet, T., Collomb, N., Faucher, M., Delon-Martin, C., Coizet, V., Achard, S., Barbier, E.L., 2020b. Functional connectivity is preserved but reorganized across several anesthetic regimes. NeuroImage 219, 116945.
- Bergholm, F., Adler, J., Parmryd, I., 2010. Analysis of bias in the apparent correlation coefficient between image pairs corrupted by severe noise. J. Math. Imaging Vis. 37, 204–219.
- Bolt, T., Nomi, J.S., Rubinov, M., Uddin, L.Q., 2017. Correspondence between evoked and intrinsic functional brain network configurations. Hum. Brain Mapp. 38 (4), 1992–2007, https://onlinelibrary.wiley.com/doi/pdf/10.1002/hbm.23500.

Braun, U., Plichta, M.M., Esslinger, C., Sauer, C., Haddad, L., Grimm, O., Mier, D., Mohnke, S., Heinz, A., Erk, S., Walter, H., Seiferth, N., Kirsch, P., Meyer-Lindenberg, A., 2012. Test-retest reliability of resting-state connectivity network characteristics using fMRI and graph theoretical measures. NeuroImage 59 (2), 1404–1412

- Büchel, C., Friston, K.J., 1997. Modulation of connectivity in visual pathways by attention: cortical interactions evaluated with structural equation modelling and fMRI. Cerebral Cortex 7 (8), 768–778.
- Burt, J.B., Helmer, M., Shinn, M., Anticevic, A., Murray, J.D., 2020. Generative modeling of brain maps with spatial autocorrelation. NeuroImage 220, 117038.
- Caballero-Gaudes, C., Reynolds, R.C., 2017. Methods for cleaning the BOLD fMRI signal. NeuroImage 154, 128–149.
- Cao, H., McEwen, S.C., Forsyth, J.K., Gee, D.G., Bearden, C.E., Addington, J., Goodyear, B., Cadenhead, K.S., Mirzakhanian, H., Cornblatt, B.A., Carrión, R.E., Mathalon, D.H., McGlashan, T.H., Perkins, D.O., Belger, A., Seidman, L.J., Thermenos, H., Tsuang, M.T., van Erp, T.G.M., Walker, E.F., Hamann, S., Anticevic, A., Woods, S.W., Cannon, T.D., 2019. Toward leveraging human connectomic data in large consortia: Generalizability of fMRI-based brain graphs across sites, sessions, and paradigms. Cerebral Cortex 29 (3), 1263–1279.
- Cao, J., Worsley, K., 1999. The geometry of correlation fields with an application to functional connectivity of the brain. Ann. Appl. Probab. 9 (4), 1021–1057, Publisher: Institute of Mathematical Statistics.
- Castellanos, F.X., Di Martino, A., Craddock, R.C., Mehta, A.D., Milham, M.P., 2013.
  Clinical applications of the functional connectome. NeuroImage 80, 527–540.
- Castrillon, J.G., Ahmadi, A., Navab, N., Richiardi, J., 2014. Learning with multi-site fMRI graph data. In: 2014 48th Asilomar Conference on Signals, Systems and Computers. pp. 608–612, ISSN: 1058-6393.
- Chen, J.E., Glover, G.H., 2015. BOLD fractional contribution to resting-state functional connectivity above 0.1 Hz. NeuroImage 107, 207–218.
- Chen, A.A., Srinivasan, D., Pomponio, R., Fan, Y., Nasrallah, I.M., Resnick, S.M., Beason-Held, L.L., Davatzikos, C., Satterthwaite, T.D., Bassett, D.S., Shinohara, R.T., Shou, H., 2022. Harmonizing functional connectivity reduces scanner effects in community detection. NeuroImage 256, 119198.
- Clifford, P., Richardson, S., Hemon, D., 1989. Assessing the significance of the correlation between two spatial processes. Biometrics 45 (1), 123–134.
- Cordes, D., Haughton, V.M., Arfanakis, K., Carew, J.D., Turski, P.A., Moritz, C.H., Quigley, M.A., Meyerand, M.E., 2001. Frequencies contributing to functional connectivity in the cerebral cortex in "resting-state" data. Am. J. Neuroradiol. 22 (7), 1326–1333, Publisher: American Journal of Neuroradiology Section: BRAIN.
- Dadi, K., Rahim, M., Abraham, A., Chyzhyk, D., Milham, M., Thirion, B., Varo-quaux, G., 2019. Benchmarking functional connectome-based predictive models for resting-state fMRI. NeuroImage 192, 115–134.
- Deco, G., Ponce-Alvarez, A., Hagmann, P., Romani, G.L., Mantini, D., Corbetta, M., 2014. How local excitation-inhibition ratio impacts the whole brain dynamics. J. Neurosci. 34 (23), 7886–7898.
- Descombes, X., Kruggel, F., Von Cramon, D., 1998. fMRI signal restoration using a spatio-temporal Markov random field preserving transitions. NeuroImage 8 (4), 340–349.
- Eickhoff, S.B., Thirion, B., Varoquaux, G., Bzdok, D., 2015. Connectivity-based parcellation: Critique and implications. Hum. Brain Mapp. 36 (12), 4771–4792.
- Fan, F., Liao, X., Lei, T., Zhao, T., Xia, M., Men, W., Wang, Y., Hu, M., Liu, J., Qin, S., Tan, S., Gao, J.-H., Dong, Q., Tao, S., He, Y., 2021. Development of the defaultmode network during childhood and adolescence: A longitudinal resting-state fMRI study. NeuroImage 226, 117581.
- Figueroa-Jimenez, M.D., Cañete-Massé, C., Carbó-Carreté, M., Zarabozo-Hurtado, D., Peró-Cebollero, M., Salazar-Estrada, J.G., Guàrdia-Olmos, J., 2021. Resting-state default mode network connectivity in young individuals with Down syndrome. Brain Behav. 11 (1), e01905, https://onlinelibrary.wiley.com/doi/pdf/10.1002/ brb3.1905
- Finn, E.S., Shen, X., Scheinost, D., Rosenberg, M.D., Huang, J., Chun, M.M., Papademetris, X., Constable, R.T., 2015. Functional connectome fingerprinting: identifying individuals using patterns of brain connectivity. Nature Neurosci. 18 (11), 1664–1671.
- Fornito, A., Bullmore, E.T., Zalesky, A., 2017. Opportunities and challenges for psychiatry in the connectomic era. Biol. Psychiatry: Cogn. Neurosci. Neuroimaging 2 (1), 9–19.
- Fornito, A., Zalesky, A., Breakspear, M., 2015. The connectomics of brain disorders. Nat. Rev. Neurosci. 16 (3), 159–172.
- Gaetan, C., Guyon, X., et al., 2010. Spatial Statistics and Modeling, Vol. 90. Springer. Glasser, M.F., Sotiropoulos, S.N., Wilson, J.A., Coalson, T.S., Fischl, B., Andersson, J.L., Xu, J., Jbabdi, S., Webster, M., Polimeni, J.R., Van Essen, D.C., Jenkinson, M., 2013. The minimal preprocessing pipelines for the Human Connectome Project. NeuroImage 80, 105–124.
- Greve, D.N., Brown, G.G., Mueller, B.A., Glover, G., Liu, T.T., Function Biomedical Research Network, 2013. A survey of the sources of noise in fMRI. Psychometrika 78 (3), 396–416.
- Greve, D.N., Mueller, B.A., Liu, T., Turner, J.A., Voyvodic, J., Yetter, E., Diaz, M., McCarthy, G., Wallace, S., Roach, B.J., Ford, J.M., Mathalon, D.H., Calhoun, V.D., Wible, C.G., Brown, G.G., Potkin, S.G., Glover, G., 2011. A novel method for quantifying scanner instability in fMRI: Quantifying scanner instability in fMRI. Magn. Reson. Med. 65 (4), 1053–1061.

- Gunst, R.F., 1995. Estimating spatial correlations from spatial-temporal meteorological data. J. Clim. 8, 2454–2469.
- Hartvig, N.V., Jensen, J.L., 2000. Spatial mixture modeling of fMRI data. Hum. Brain Mapp. 11 (4), 233–248.
- Jiang, L., Zuo, X.-N., 2016. Regional homogeneity: A multimodal, multiscale neuroimaging marker of the human connectome. Neuroscientist 22 (5), 486–505.
- Jo, H.J., Saad, Z.S., Simmons, W.K., Milbury, L.A., Cox, R.W., 2010. Mapping sources of correlation in resting state FMRI, with artifact detection and removal. NeuroImage 52 (2), 571–582.
- Köhler, S., McIntosh, A.R., Moscovitch, M., Winocur, G., 1998. Functional interactions between the medial temporal lobes and posterior neocortex related to episodic memory retrieval. Cerebral Cortex 8 (5), 451–461.
- Lazar, N.A., 2008. Noise and data preprocessing. In: The Statistical Analysis of Functional MRI Data. In: Statistics for Biology and Health, Springer New York, New York, NY, pp. 37–51, ISSN: 1431-8776.
- Lin, L.I.-K., 1989. A concordance correlation coefficient to evaluate reproducibility. Biometrics 45 (1), 255–268, Publisher: [Wiley, International Biometric Society].
- Liu, T.T., 2016. Noise contributions to the fMRI signal: An overview. NeuroImage 143, 141–151.
- Markello, R.D., Misic, B., 2021. Comparing spatial null models for brain maps. NeuroImage 236, 118052.
- Moulines, E., Roueff, F., Taqqu, M.S., 2007. On the spectral density of the wavelet coefficients of long-memory time series with application to the log-regression estimation of the memory parameter. J. Time Series Anal. 28 (2), 155–187.
- Murphy, K., Birn, R.M., Bandettini, P.A., 2013. Resting-state fMRI confounds and cleanup. NeuroImage 80, 349–359.
- Ng, B., Varoquaux, G., Poline, J.B., Greicius, M., Thirion, B., 2016. Transport on Riemannian manifold for connectivity-based brain decoding. IEEE Trans. Med. Imaging 35 (1), 208–216.
- Ogawa, A., 2021. Time-varying measures of cerebral network centrality correlate with visual saliency during movie watching. Brain Behav. 11 (9), e2334, https://onlinelibrary.wiley.com/doi/pdf/10.1002/brb3.2334.
- Ostroff, C., 1993. Comparing correlations based on individual-level and aggregated data. J. Appl. Psychol. 78 (4), 569.
- Pawela, C.P., Biswal, B.B., Cho, Y.R., Kao, D.S., Li, R., Jones, S.R., Schulte, M.L., Matloub, H.S., Hudetz, A.G., Hyde, J.S., 2008. Resting-state functional connectivity of the rat brain. Magn. Reson. Med. 59 (5), 1021–1029.
- Petersen, A., Zhao, J., Carmichael, O., Müller, H.-G., 2016. Quantifying individual brain connectivity with functional principal component analysis for networks. Brain Connect. 6 (7), 540–547.
- Poline, J.B., Worsley, K.J., Evans, A.C., Friston, K.J., 1997. Combining spatial extent and peak intensity to test for activations in functional imaging. NeuroImage 5 (2), 83–96.
- Poline, J.-B., Worsley, K.J., Holmes, A.P., Frackowiak, R.S.J., Friston, K.J., 1995. Estimating smoothness in statistical parametric maps: Variability of p values. J. Comput. Assist. Tomogr. 19 (5), 788–796.
- Richiardi, J., Achard, S., Bunke, H., Van De Ville, D., 2013. Machine learning with brain graphs: Predictive modeling approaches for functional imaging in systems neuroscience. IEEE Signal Process. Mag. 30 (3), 58–70.
- Rosner, B., Donner, A., Hennekens, C., 1977. Estimation of interclass correlation from familial data. Appl. Stat. 26, 179–187.

- Salvador, R., Suckling, J., Schwarzbauer, C., Bullmore, E., 2005. Undirected graphs of frequency-dependent functional connectivity in whole brain networks. Philos. Trans. B. Soc. B 360 (1457), 937–946.
- Stanley, M.L., Moussa, M.N., Paolini, B.M., Lyday, R.G., Burdette, J.H., Laurienti, P.J., 2013. Defining nodes in complex brain networks. Front. Comput. Neurosci. 7.
- Student, 1914. The elimination of spurious correlation due to position in time and space. Biometrika 10, 179–181.
- Termenon, M., Jaillard, A., Delon-Martin, C., Achard, S., 2016. Reliability of graph analysis of resting state fMRI using test-retest dataset from the Human Connectome Project. Neuroimage 142, 172–187.
- Tomasi, D., Volkow, N.D., 2010. Functional connectivity density mapping. Proc. Natl. Acad. Sci. 107 (21), 9885–9890.
- Tooley, U.A., Bassett, D.S., Mackey, A.P., 2021. Environmental influences on the pace of brain development. Nat. Rev. Neurosci. 22 (6), 372–384.
- Triana, A.M., Glerean, E., Saramäki, J., Korhonen, O., 2020. Effects of spatial smoothing on group-level differences in functional brain networks. Netw. Neurosci. 4 (3), 556–574.
- Uddin, L.Q., Kelly, A.C., Biswal, B.B., Margulies, D.S., Shehzad, Z., Shaw, D., Ghaffari, M., Rotrosen, J., Adler, L.A., Castellanos, F.X., Milham, M.P., 2008. Network homogeneity reveals decreased integrity of default-mode network in ADHD. J. Neurosci. Methods 169 (1), 249–254.
- Van Dijk, K.R.A., Hedden, T., Venkataraman, A., Evans, K.C., Lazar, S.W., Buckner, R.L., 2010. Intrinsic functional connectivity as a tool for human connectomics: Theory, properties, and optimization. J. Neurophysiol. 103 (1), 297–321.
- Whitlow, C.T., Casanova, R., Maldjian, J.A., 2011. Effect of resting-state functional MR imaging duration on stability of graph theory metrics of brain network connectivity. Radiology 259 (2), 516–524.
- Wilson, D.J., 2019. The harmonic mean p -value for combining dependent tests. Proc. Natl. Acad. Sci. 116 (4), 1195–1200.
- Worsley, K.J., Evans, A.C., Marrett, S., Neelin, P., 1992. A three-dimensional statistical analysis for CBF activation studies in human brain. J. Cereb. Blood Flow Metab. 12 (6), 900–918, Publisher: SAGE Publications Ltd STM.
- Worsley, K.J., Marrett, S., Neelin, P., Vandal, A.C., Friston, K.J., Evans, A.C., 1996. A unified statistical approach for determining significant signals in images of cerebral activation. Hum. Brain Mapp. 4 (1), 58–73, eprint: https://onlinelibrary.wiley.com/doi/pdf/10.1002/%28SICI%291097-0193%281996%294%3A1/%3C58%3A%3AAID-HBM4%3E3.0.CO%3B2-O.
- Yan, C.-G., Cheung, B., Kelly, C., Colcombe, S., Craddock, R.C., Di Martino, A., Li, Q., Zuo, X.-N., Castellanos, F.X., Milham, M.P., 2013. A comprehensive assessment of regional variation in the impact of head micromovements on functional connectomics. NeuroImage 76, 183–201.
- Ye, J., Lazar, N.A., Li, Y., 2009. Geostatistical analysis in clustering fMRI time series. Stat. Med. 28 (19), 2490–2508.
- Ye, J., Lazar, N., Li, Y., 2011. Sparse geostatistical analysis in clustering fMRI time series. J. Neurosci. Methods 199, 336–345.
- Zang, Y., Jiang, T., Lu, Y., He, Y., Tian, L., 2004. Regional homogeneity approach to fMRI data analysis. NeuroImage 22 (1), 394–400.
- Zhang, C., Cahill, N., Arbabshirani, M., White, T., Baum, S., Michael, A., 2016. Sex and age effects of functional connectivity in early adulthood. Brain Connect. 6.